CM²

MAGAZINE

第 42 期

南方科技大学海洋磁学中心主编

创刊词

海洋是生命的摇篮，是文明的纽带。地球上最早的生命诞生于海洋，海洋里的生命最终进化成了人类，人类的文化融合又通过海洋得以实现。人因海而兴。

人类对海洋的探索从未停止。从远古时代美丽的神话传说，到麦哲伦的全球航行，再到现代对大洋的科学钻探计划，海洋逐渐从人类敬畏崇拜幻想的精神寄托演变成可以开发利用与科学研究的客观存在。其中，上个世纪与太空探索同步发展的大洋科学钻探计划将人类对海洋的认知推向了崭新的纬度：深海（deep sea）与深时（deep time）。大洋钻探计划让人类知道，奔流不息的大海之下，埋藏的却是亿万年的地球历史。它们记录了地球板块的运动，从而使板块构造学说得到证实；它们记录了地球环境的演变，从而让古海洋学方兴未艾。

在探索海洋的悠久历史中，从大航海时代的导航，到大洋钻探计划中不可或缺的磁性地层学，磁学发挥了不可替代的作用。这不是偶然，因为从微观到宏观，磁性是最基本的物理属性之一，可以说，万物皆有磁性。基于课题组的学科背景和对海洋的理解，我们对海洋的探索以磁学为主要手段，海洋磁学中心因此而生。

海洋磁学中心，简称 CM^2，一为其全名“Centre for Marine Magnetism”的缩写，另者恰与爱因斯坦著名的质能方程 $E = MC^2$ 对称，借以表达我们对科学巨匠的敬仰和对科学的不懈追求。

然而科学从来不是单打独斗的产物。我们以磁学为研究海洋的主攻利器，但绝不仅限于磁学。凡与磁学相关的领域均是我们关注的重点。为了跟踪反映国内外地球科学特别是与磁学有关的地球科学领域的最新研究进展，海洋磁学中心特地主办 CM^2 Magazine，以期与各位地球科学工作者相互交流学习、合作共进！

“海洋孕育了生命，联通了世界，促进了发展”。 21 世纪是海洋科学的时代，由陆向海，让我们携手迈进中国海洋科学的黄金时代

目 录

研究进展 1

Nature Communications: 亚洲大陆气候在 3400 万年前南极冰盖扩张时的气候变化 1

EPSL: 埃迪卡拉纪晚期阿瓦隆地块古地理位置重建和西冈瓦纳大陆的寒武纪聚合 3

海磁快讯 5

海洋磁学中心携新成果在 2020 年中国海洋经济博览会首次亮相 5

海洋磁学中心师生参加 2020 中国地球科学联合学术年会 7

岩石磁学演绎 8

第 32 章　单一磁性参数总结 8

文献速递 14

1. 末次冰期以来南大洋大象岛沿岸的古海洋研究：对海表生产力，营养盐利用率，底流和冰筏碎屑之间联系的指示 14
2. 古新世-始新世边界温度与碳酸盐共同演化：来自印度洋低纬度微量元素新纪录 18
3. 超深金刚石记录了岩石圈至下地幔的碳循环过程 23
4. Futuna 岛东南部广泛分布的火山：近海底磁异常定年和区域性的结果 25
5. 2005 年至 2010 年南部非洲南大西洋异常的演变：基于地面和卫星数据的谐波样条磁场主磁场模型 27
6. 新几内亚西北部新生代岩浆活动和碰撞历史为澳大利亚板块最北缘的构造演化提供了新的视角 29

7. 古地磁约束 Nuna 超大陆核心澳大利亚-劳伦古陆连接的持续时间.....33

8. 晚第四纪东亚非均质降雨变化对哈德利环流重组的响应.....35

9. 从一阶反转曲线推断深海沉积物静磁相互作用:相对古强度归一化的意义...39

10. 马尔马拉海沉积物在过去 70 ka 来的高分辨率古地磁记录.....42

11. 非人为沉积物重建的洞穴演化史有助于我们理解相关的考古背景.....44

12. 26 ka 以来中亚的干湿演化:来自西部天山吉尔吉斯黄土剖面的见解.....46

13. 全球温度模式揭示了全新世温度难题.....49

研究进展

Nature Communications: 亚洲大陆气候在 3400 万年前南极冰盖扩张时的气候变化

3400万年前的始新世-渐新世气候转型（Eocene–Oligocene transition）是新生代气候演化过程中最显著的变冷事件之一，它伴随着南极大陆冰盖的出现，标志着地球从两极无冰的“温室地球”转变成了南极有冰的“冰室地球”。这一转变伴随着一系列巨大地球环境变化，使得地球上的生命经历了一次严峻的挑战，进而地球上的现代生物得以起源。

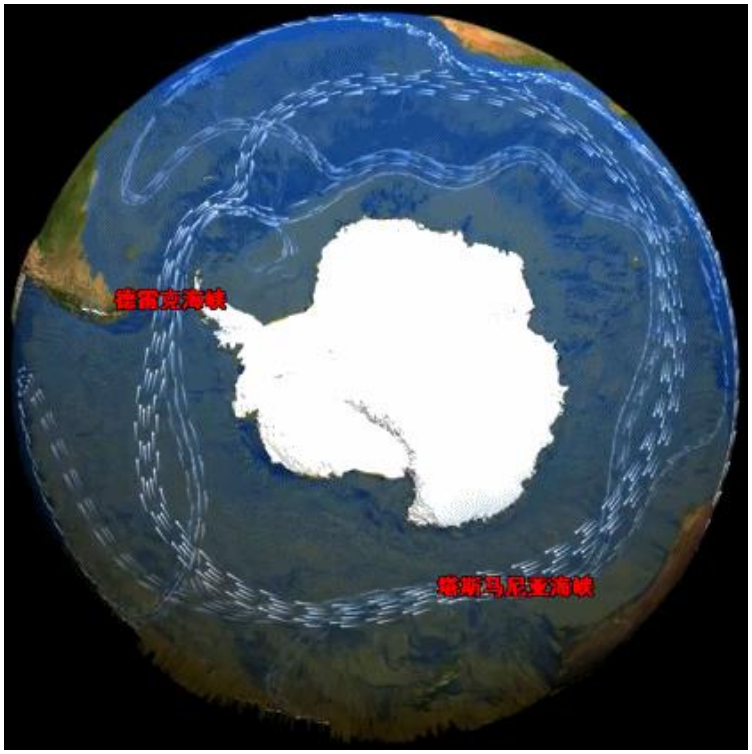

南极冰盖形成和伴随的大洋环流变化

那么，南极冰盖在3400万年前究竟是如何形成的？在这次气候转型过程中各个气候系统伴随着怎样的变化特征？尤其是在轨道尺度上是如何变化的？这些科学问题一直是古气候学研究的热点。近日，由中国科学院地球环境研究所安芷生院士、敖红研究员和张鹏博士、南方科技大学海洋磁学中心刘青松教授、香港大学柳中晖副教授等组成的中国研究团队联合法国雷恩第一大学和澳大利亚国立大学等国际研究团队，在始新世-渐新世气候转型过程中的轨道周期变化研究方面取得新进展，揭示出这一气候转型伴随着轨道周期的变化，为进一步研究这次南极冰盖形成的动力学机制及其全球环境和生物效应提供了新材料。

研究人员结合磁性地层学和天文年代学确定了中国西部兰州地区晚始新世

至早渐新世河湖相沉积地层的准确年代，通过综合的环境磁学和元素地球化学重建了3550–3100万年的高分率气候记录。该记录有效跨越了始新世-渐新世气候转型阶段，结果表明在始新世-渐新世转型南极冰盖大幅扩张时兰州盆地气候不仅显著变得干旱，而且气候的轨道周期存在转型。在3370万年前，南极冰盖规模较小时，兰州盆地气候的轨道周期由偏心率（40万年和10万年）主导；而在3370万年后，南极形成巨大冰盖时，兰州盆地气候的轨道周期则表现出综合的偏心率（40万年和10万年）、斜率（4万年）和岁差（2万年）周期，并伴随着斜率的振幅调制周期（120万年）。通过海陆综合对比，研究团队认为在始新世-渐新世转型时亚洲大陆气候的轨道周期转型和干旱化的趋势变化可能与同时代大气CO_2浓度降低和南极冰盖大规模形成等边界条件有关。

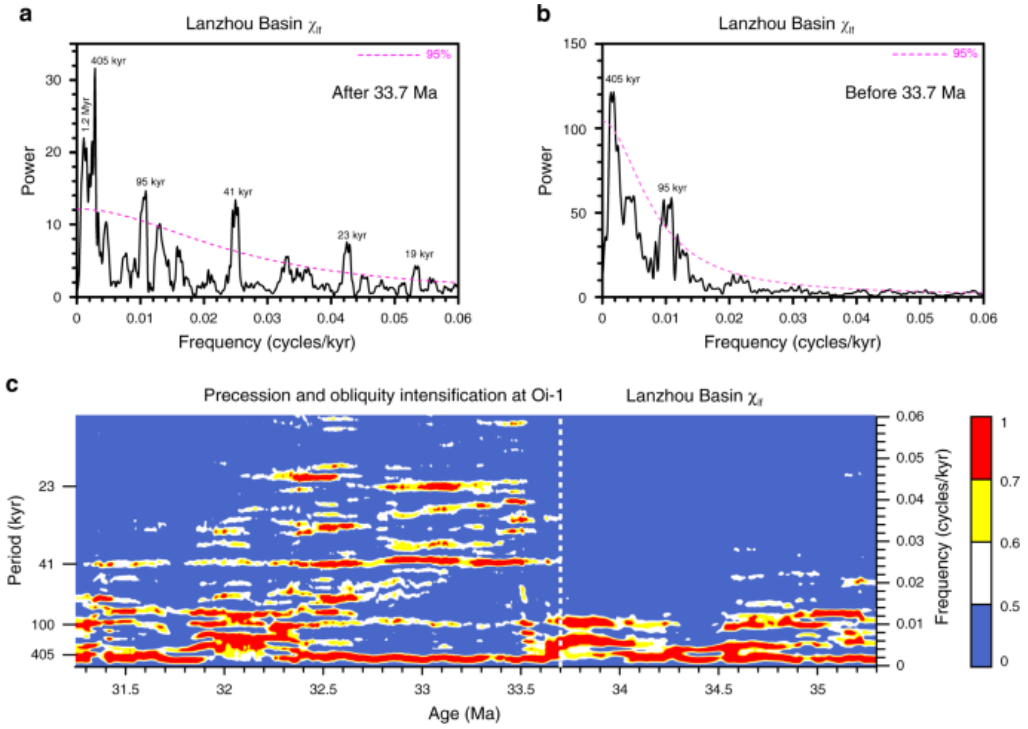

兰州盆地磁化率记录的轨道周期气候变化

该研究成果于近期以 Article 形式发表在 Nature Communications (Ao, H., et al., 2020. Orbital climate variability on the northeastern Tibetan Plateau across the Eocene–Oligocene transition. Nature Communications 11: 5249)。该研究得到中国科学院战略重点研究计划、第二次青藏科考计划、中国科学院前沿科学重点研究项目、国家自然科学基金和科技部的联合资助。

作者简介：敖红，男，中科院地球环境研究所研究员，以第四纪地质学和地球物理学等学科交叉为基础，从事新生代磁性地层学、环境磁学和古气候学的综合研究， 2014 年入选首批中国科学院卓越青年科学家。

EPSL：埃迪卡拉纪晚期阿瓦隆地块古地理位置重建和西冈瓦纳大陆的寒武纪聚合

地球历史上超大陆旋回演化对地球系统的各个圈层，包括岩石圈、水圈、大气圈和生物圈等都有着深刻影响（Nance et al., 2014），且多个研究表明，地球表面每经历约 5-7 亿年就会形成一个超大陆，如可能存在的 Kenorland (2500-2100 Ma)、Nuna (1600-1400 Ma)、Rodinia (900-700 Ma)以及未来可能形成的 Amasia 超大陆（e.g., Mitchell et al., 2012; Evans et al., 20-16; Li et al., 2019）。但是作为地球演化历史中比较特殊的埃迪卡拉纪时期，有学者认为还可能存在另一个超大陆——Pannotia（Dalziel, 1997）。自 Pannotia 超大陆假说提出以来，一直饱受争议（Evans, 2020; Murphy et al., 2020）,一个很核心的争议就发生在冈瓦纳大陆西部，作为西冈瓦纳主要组成板块之一的亚马逊板块是否在这一时期与其他核心冈瓦纳（通过泛非运动聚合形成中冈瓦纳）部分发生最终拼合（e.g., Trindade et al., 2006; Tohver et al., 2010, 2012; Cordani et al., 2013; McGee et al., 2015; Schmitt et al., 2018）。造成这一争议的一个重要原因就是相关块体地质记录的不充分和可靠古地磁数据的缺乏（D'Agrella-Filho et al., 2016）。

针对这一科学问题，我们选择对亚马逊（Amazonia）板块相关块体——阿瓦隆(Avalonia)地块（也是见证了从冈瓦纳大陆至 Pangea 超大陆聚合的泛冈瓦纳块体）保存的具有良好年龄约束的埃迪卡拉纪（ca. 590-560 Ma）地层进行古地磁研究，研究区位于加拿大纽芬兰岛（图 1）。本次研究分别获得 ca. 590 和 560 Ma 两个可靠古地磁极（通过褶皱检验和倒转检验），并结合这一时期其他主要相邻板块，包括劳伦（Laurentia）、西非（West Africa）及波罗地（Baltica）的可靠古地磁极对西冈瓦纳的古地理位置进行了定量重建（图 2）。通过本次研究我们取得以下认识：

1） 西冈瓦纳大陆并未在埃迪卡拉纪时期完成最终拼合，阿瓦隆-亚马逊（Avalonia-Amazonia）板块与中冈瓦纳之间被大洋（称为 Clymene Ocean）隔开，结合相关地质证据表明其最终拼合发生在寒武纪早期。因此，埃迪卡拉纪 Pannotia 超大陆不存在；

2） 进一步验证了 590-560Ma 时期真极移事件发生的可能性;本研究为研究从 Rodinia 至冈瓦纳大陆形成的超大陆转换时期提供了一个关键的初步约束，进一步解决埃迪卡拉纪时期全球古地理重建及动力学演化问题还有待进一步研究。

本研究受到耶鲁大学博士后项目和中国地质大学"百人计划"项目（温斌）、牛津大学和 NASA（(NNX14AP10H)）项目（Ross P. Anderson）以及加拿大 NSERC–Discovery 项目（Phil J. A. McCausland）共同资助。第一阶段成果已发表在 Earth and Planetary Science Letters 期刊上： Wen, B., Evans, D.A.D., Anderson, R. P., and McCausland, P. J.A., 2020. Late Ediacaran paleogeography of Avalonia and the Cambrian assembly of West Gondwana. Earth and Planetary Science Letters, https://doi.org/10.1016/j.epsl.2020.116591 。

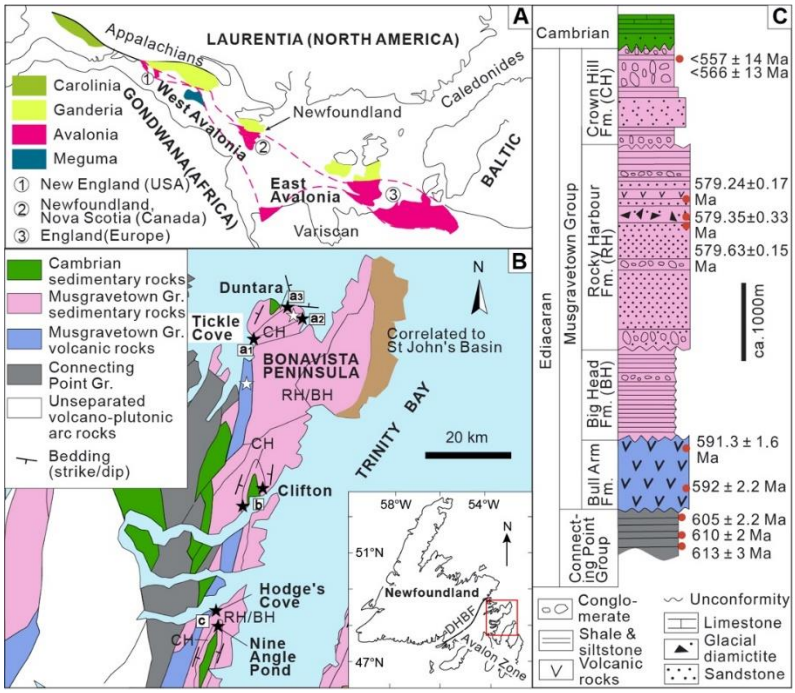

图 1. 阿瓦隆地块及本研究区地质及样品采点示意图，星号 代表取样点。

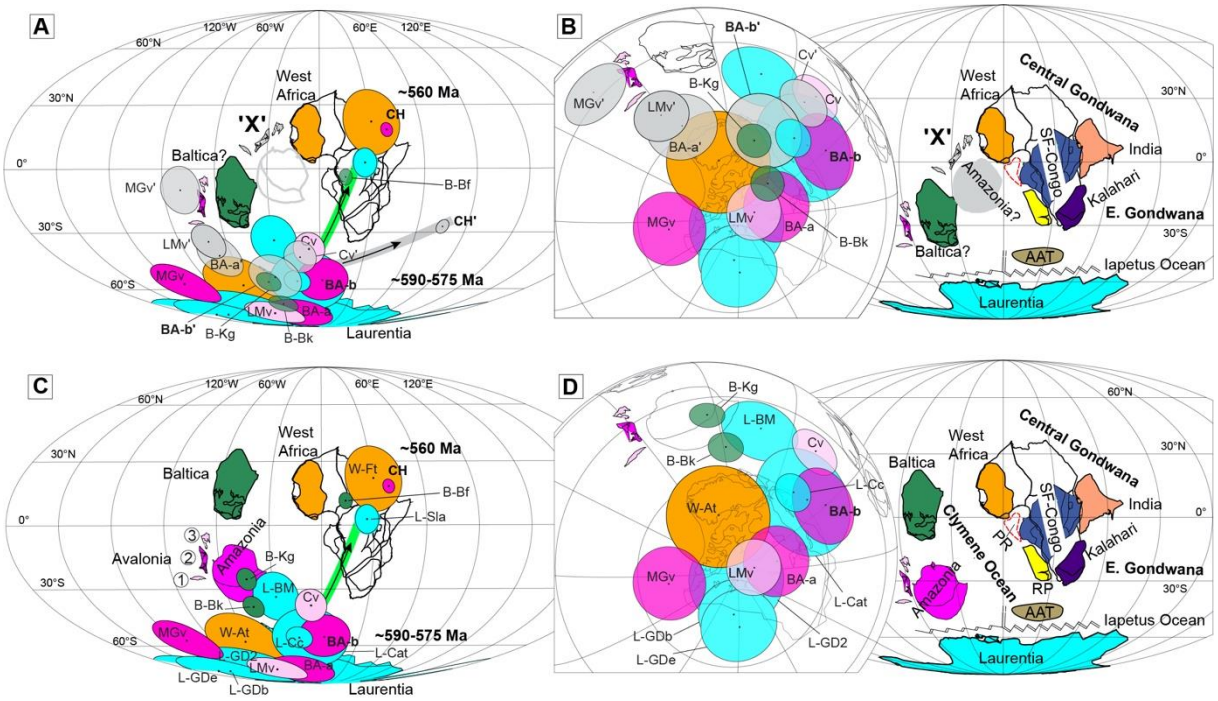

图 2. 埃迪卡拉纪晚期真极移框架下西冈瓦纳重建示意图。（SF =São Francisco; RP =Río de La Plata; PR =Parnaíba; AAT =Arequipa-Antofalla Terrane）。

作者简介：温斌，中国地质大学（武汉），主要从事古地磁及古大陆/超大陆重建及动力学演化；David A. D. Evans，美国耶鲁大学；Ross P. Anderson，英国牛津大学；Phil J. A. McCausland，加拿大韦仕敦大学。

海磁快讯

海洋磁学中心携新成果在 2020 年中国海洋经济博览会首次亮相

2020 年 10 月 15－18 日，以“开放合作、共赢共享”为主题的 2020 中国海洋经济博览会（以下简称“海博会”）在深圳会展中心举行，海洋磁学中心携新成果在南方科技大学海洋科学与工程系的组织下，首次亮相中国海洋经济博览会大舞台。

海博会是中国唯一的国家级国际性海洋经济展会，也是全新的对外展示中国海洋经济发展成果的重要窗口、世界沿海国家开放合作、共赢共享的重要平台、推进海洋新技术成果转化和产业化的重要功能平台、促进海洋经济国际合作的高端经贸平台。

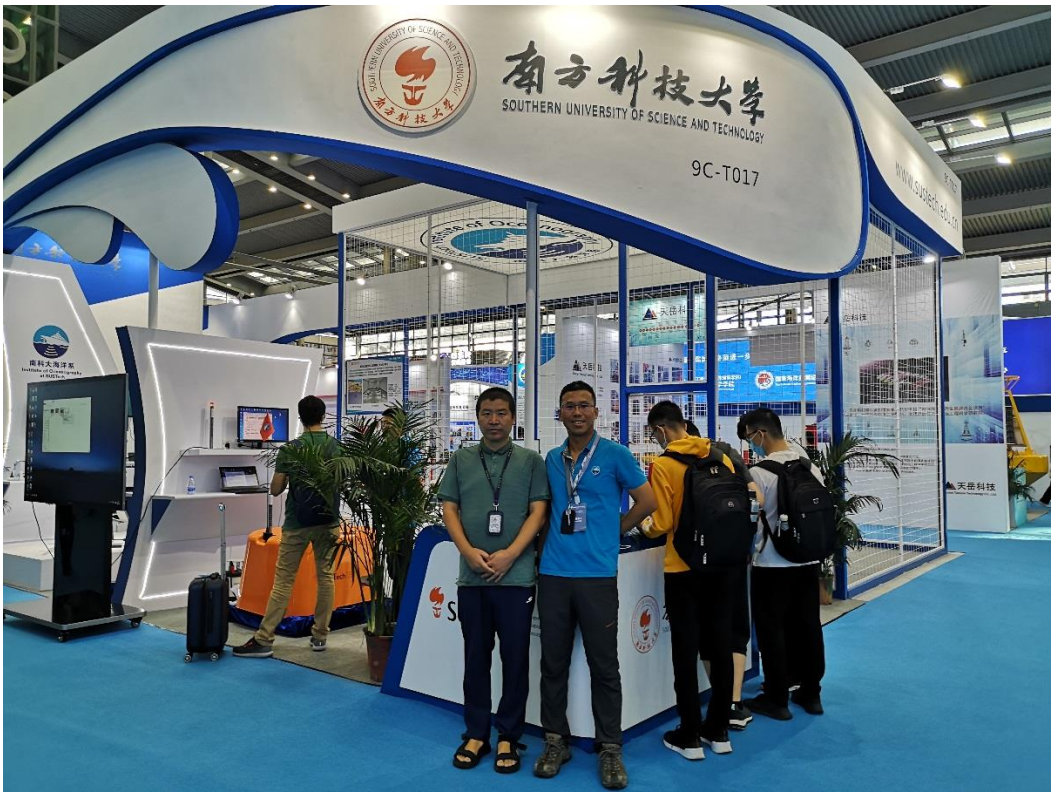

海洋磁学中心主任刘青松讲席教授和副主任周祐民助理教授亲临现场

海洋磁学中心此次亮相的创新成果有：垂起固定翼无人机光泵及磁通门航磁系统（VTOL Fixed-wing UAV Aeromagnetic Survey System）、多旋翼无人机光泵及磁通门航磁系统（MultiCopter Aeromagnetic Survey System）和油电混动四旋翼无人机吊舱系统（Gas-electric Hybrid Quadcopter UAV Aeromagnetic Survey System）。

垂起固定翼无人机航磁系统不受水域、森林、沼泽、沙漠和高山等地形条件限制，具效率高、成本低、便于大面积工作、探测深度较大等优点，适合大面积，平缓地形或海洋移动平台作业。CW-15 垂起固定翼无人机光泵及磁通门航磁系统入选 2019 年度中国海洋十大科技进展。在南海北部珠江口海域执行了无人机

海上航磁探测的试验任务，海试中在配备了磁通门和光泵磁力仪集成技术 GTK-R15M 型垂起固定翼无人机上，进行了地磁海空联测。海试成果亮点：一是取得了“空-海域地磁场联测”技术“从无到有”的重大突破；二是实现了无人机在移动平台上的精准起降，与船磁测量同步作业的技术方法。“空-海域” 地磁场联测的结果与早期磁测成果的形态相似，但细节更丰富。

多旋翼无人机光泵及磁通门航磁系统和油电混动四旋翼无人机吊舱系统为行业用户提供了航磁航测一站式解决方案，能超低空作业，有灵活机动、高效快速、精细准确，作业成本低、生产周期短等特点，可在一定程度上突破自然条件和人类能力限制、代替地面工作人员进行远距离（难以到达）和高危地区作业，能够在复杂地面和气象条件下执行飞行任务，实现了低风险、低成本、高质量航空物探测量作业。为地质找矿、工程勘察和环境调查工作提供高效快速的技术装备。应用范围:矿业探测（铁矿、金矿、铜矿、 锡矿、钴石等）、工程地质勘察（高铁、隧道、桥梁等）、海洋物探调查、军事、考古、UXO（未爆弹药）探测和与地磁相关的科学与地球物理探测等。

参展的无人机航磁系统

海洋磁学中心主任刘青松讲席教授表示，研究团队将努力探索海洋磁学发展的新方向，充分发挥学科交叉、集成创新和产学研协同合作的特色与科研优势，加强与行业优秀企业的合作，研发出更多的科技创新成果，为深圳建设全球海洋中心城市、为建设海洋强国贡献力量。

海洋磁学中心师生参加 2020 中国地球科学联合学术年会

2020 年 10 月 17－21 日，第七届中国地球科学联合学术年会在重庆召开。海洋磁学中心师生十余人参加会议，并做口头报告和展板报告。

海洋磁学中心师生合影

各位参会成员所做报告如下：

周祐民助理教授—口头报告—《Co -Seismic Focal Mechanism of 1999 Chi-Chi Earthquake (1999, Taiwan, Mw 7.6) Deduced from Gouge Magnetic Fabric》。

仲义研究助理教授—口头报告—《晚第四纪以来高低纬度气候体系在北太平洋地区的响应特征研究》。

蒋晓东研究助理教授—口头报告—《西太平洋锰结核化石磁小体特征及对成矿的指示意义》。

柳加波博士后—口头报告—《70ka 以来黑海古地磁记录的 Nowegian - Greenland Sea、Laschmaps 和 Mono Lake 地磁漂移事件》。

李园洁博士后—口头报告—《海洋磁异常记录的白垩纪超静期间地场古强度变化》。

冯婉仪博士后—展板报告—《西天山新源地区早石炭世大陆弧岩浆的地幔源区特征》。

博士生刘伟—口头报告—《菲律宾海四国盆地 ODP 1177 孔古地磁学和沉积物源的初步研究》。

本次参会，展现了海洋磁学中心的最新研究成果，促进了与全国同行的学术交流。祝愿中国地球科学联合学术联会越办越好，祝愿《古地磁学与地球动力学》专题的各位同行的学术道路越走越宽广！

第 32 章　单一磁性参数总结

岩石磁学参数和磁性颗粒的种类、磁畴状态以及含量等因素密切相关。这些因素又和地质过程紧密相连。因此，在特定的之环境中，我们就有可能把岩石磁学参数和地质过程联系起来。

岩石磁学参数众多，我们先总结一下常见的单一磁性参数。

磁化率单位为 m^3kg^{-1}:

$\chi_{low\text{-}field}$	低场磁化率
$\chi_{hifi\text{-}field}$	高场磁化率
χ_{ferri}	铁磁性磁化率（$\chi_{low\text{-}field} - \chi_{hifi\text{-}field}$ ）
χ_{lf}	低频磁化率
χ_{hf}	高频磁化率
χ_{fd}	频率磁化率（$\chi_{lf} - \chi_{hf}$）
χ_{ARM}	ARM 磁化率 ＝ARM / DC 场

剩磁参数的单位为 Am^2kg^{-1}：

SIRM	饱和等温剩磁
ARM	非磁滞剩磁
TRM	热剩磁
HIRM	SIRM 中的硬磁组分

磁滞回线参数：

M_s	饱和磁化强度
M_{rs}	饱和等温剩磁
B_c	矫顽力
B_{cr}	剩磁矫顽力
MDF	退掉一半剩磁需要的 AF 峰值场，与剩磁矫顽力相关
$B_{c\text{-}FORC}$	FORC 图中峰值密度对应的矫顽力

磁学参数给出了磁性矿物浓度、颗粒磁畴状态（或间接的磁性颗粒尺寸）以

及磁颗粒的矿物学性质，所有这些都涉及到最初的环境地质或者后续的环境过程。许多磁性参数的物理解释在此前已经有了很好的总结 [e.g., Thompson and Oldfield, 1986; Hunt et al., 1995a; Verosub and Roberts, 1995; Dekkers, 1997; Dunlop and Özdemir, 1997; Walden et al., 1999; Maher and Thompson, 1999; Peters and Dekkers, 2003; Evans and Heller, 2003; Liu et al., 2007a; Tauxe, 2010]。

低场磁化率是使用最广泛的磁性参数之一（χ 代表质量磁化率，或者κ 代表体积磁化率），定义为材料的磁响应（或感应磁化 M）与外加磁场（H）之间的比值，$\chi = dM/dH$。与剩磁不同，所有的物质对于磁化率均有贡献。因此，尽管磁化率应用广泛，但它是一个很复杂的参数，包含了多种矿物的贡献。包括强剩磁物质（即铁磁性物质，如磁铁矿、磁赤铁矿），弱剩磁物质（即反铁磁性物质，如赤铁矿、针铁矿），以及一些“非磁性”物质，包括顺磁性物质（如硅酸盐、粘土）和抗磁性物质（如石英、碳酸钙）。因此，为了能表征亚铁磁性矿物（如磁铁矿、磁黄铁矿、胶黄铁矿）的磁化率，需要扣除顺磁性物质和缺陷反铁磁性物质（如赤铁矿和针铁矿）对磁化率的贡献。亚铁磁性矿物趋向于在较高的外加磁场获得饱和。而饱和场下的磁化率（即高场磁化率，χ_{high}）可以用来指示非磁性物质的贡献（即顺磁性矿物和抗磁性矿物的贡献）。因此，我们可以得到亚铁磁性的磁化率：$\chi_{ferri} = \chi - \chi_{high}$。$\chi_{ferri}$ 依赖于磁性矿物粒径，这是由于影响磁化率强弱的自旋结构效应同样依赖于磁性矿物的粒径大小和形状。例如，对于几百纳米的磁铁矿颗粒，其内部磁结构将会分解为多个均匀一致的磁化区域（磁畴），以降低整体的磁能 [Dunlop and Özdemir, 1997; Tauxe, 2010]。磁畴壁通过在晶体内的迁移来应对不断变化的外部磁场和温度条件。因此，具有磁畴壁的多畴（MD）颗粒和无磁畴壁的一致磁化的单畴（SD）颗粒对于外场的响应是不同的。在粒度谱最小端，SD 颗粒的磁矩被限制在了特定的方向，这也限制了它们的磁化率大小。但最小的 SD 颗粒受到热波动的影响强烈，它们的磁矩也不再受到限制，这使它们表现出了一种被称为超顺磁性（SP）的行为，并具有比 SD 颗粒更高的χ。对于水热法生长的晶粒尺寸大于 100 nm 的磁铁矿颗粒，Heider et al. [1996]发现，χ不受粒径的影响，这可能是因为这些颗粒的内部压力比天然矿物较低导致的。

磁矩对外部磁场的响应能力取决于时间和温度的影响。因此，χ 依赖于所使用的测量频率或测量的时间长度。一般来说，MD 和 SD 颗粒的磁性能反映了本

质不同的磁化机制：MD 颗粒磁化受到成核作用、粒子的湮灭和畴壁运动的影响，而 SD 颗粒的磁化则是由磁化强度矢量的旋转运动引起的。因此，MD 和 SD 颗粒可以很容易区分。然而，SP 和 MD 颗粒的磁学特征有许多相似之处，因为它们不如 SD 颗粒性质稳定，并且指示粗颗粒与细颗粒存在的环境过程是千差万别的，因此，在环境磁学研究中从 MD 颗粒中明确区分出 SP 是至关重要的（见下文）。

一个中等大小的颗粒，太小不足以分成多个磁畴，但太大不足以被均匀磁化，于是表现出复杂的电子自旋模式，磁性颗粒会形成一个近似畴壁形态主导的结构，称作“旋涡”状态，而不是由畴壁分隔成两个磁畴 [*Schabes and Bertram*, 1988; *Williams and Dunlop*, 1989]，更小的颗粒可能产生“花状”结构。这些表现出了介于 MD 和 SD 颗粒之间过渡行为的颗粒，被称为假单畴（PSD）颗粒 [e.g., *Stacey*, 1962; *Stacey and Banerjee*, 1974; *Williams and Dunlop*, 1995]。

SD、PSD 或 MD 内部的自旋构造意味着，χ_{ferri} 会稍微受到晶粒尺寸的影响（图 1），以及强磁性矿物浓度的影响[*Peters and Dekkers*, 2003]。当粒径接近 SP/SD 边界（约 20-25 nm 的磁铁矿）[*Maher*, 1988; *Worm*, 1998]时，磁性变得更加复杂。粒子从稳定的 SD 颗粒转变为 SP 颗粒有一个阈值时间，如果观测频率足够高，就可以观测到颗粒对外场的响应，因此这一粒径区域同时受时间和温度的影响。通过降低温度或观察的时间跨度， SP/SD 边界以下的颗粒可以从 SP 状态改变为稳定的 SD 状态 [*O'Reilly*, 1984; *Worm*, 1998]。在实践中，这可以通过增加观测频率来实现（例如，从 470 Hz 到 4700 Hz，这是两个常用 Bartington 磁化率仪的工作频率）。从 SP 到稳定的 SD 状态的改变，会导致χ的急剧下降[*Thompson and Oldfield*, 1986; *Worm*, 1998; *Till et al*., 2011]。因此，绝对频率磁化率χ_{fd} (= $\chi_{470\ Hz}$ - $\chi_{4700\ Hz}$)可以用来确定 SP/SD 边界颗粒的含量 [*Liu et al*., 2005a]。用χ_{ferri} 对χ_{fd} 进行归一化，可得到χ_{fd}% （=$\chi_{fd}/\chi_{ferri}\times 100\%$)。$\chi_{fd}$ 和χ_{fd}%都可以用于检测 SP 颗粒的存在[*Zhou et al*., 1990; *Worm*, 1998; *Liu et al*., 2005a]。χ_{fd}%还与 SP/SD 边界处粒子集的分布形态有关 [*Worm*, 1998]。SP 的行为具有极强的温度依赖性，这意味着测量χ随温度变化的函数是非常有意义的[e.g., *Dunlop*, 1973; *Liu et al.*, 2005a]。

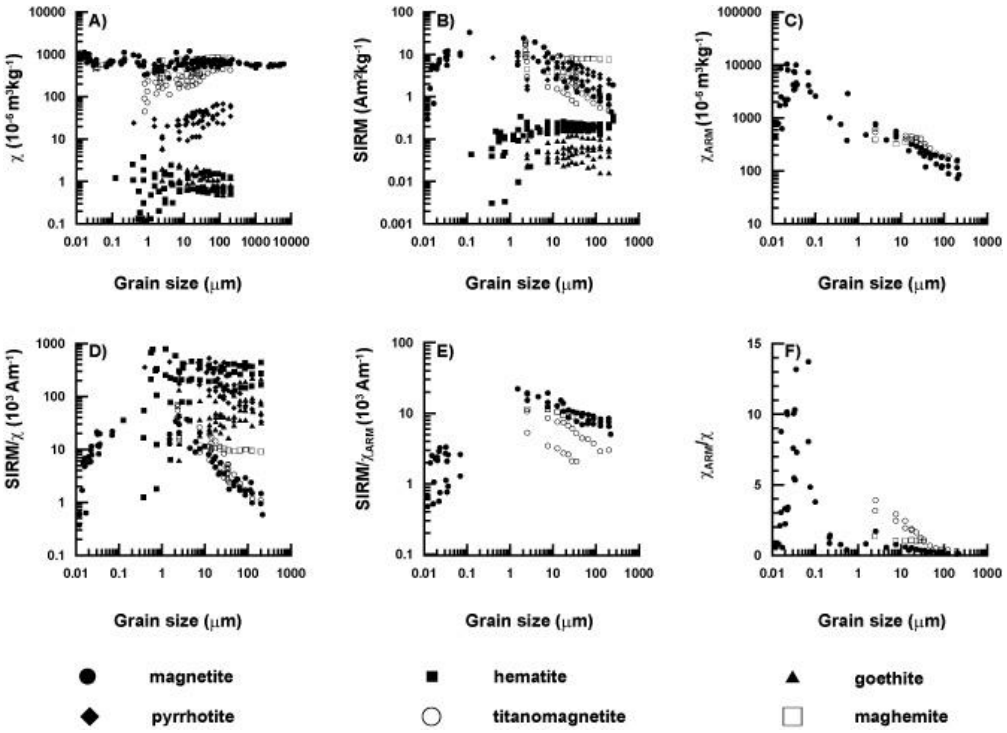

图 1 不同磁学参数与粒径的相关图 (修改自 *Peters and Dekkers* [2003])

稳定的 SD 颗粒具有最低的χ_{ferri}，但却有最高的记录剩磁的能力[*Banerjee et al*., 1981; *King et al*., 1982; *Hunt et al*., 1995a]。通过给样品施加一个交变场 (e.g., AF = ~100 mT) 再叠加一个小的直流场 (e.g., DC = ~50 T)，可以获得样品的非磁滞剩磁（ARM）。ARM 的大小与直流偏转场成比例，因此经常以 ARM 的磁化率形式 (χ_{ARM} = ARM/DC bias field) 出现。

一般情况下，ARM 主要反应 SD 颗粒的含量变化。

虽然 ARM 是一个有用的参数，但对 ARM 的解释仍存在一定的复杂性。例如，χ_{ARM} 和 χ_{fd}(或χ_{fd}%)对于 SP 和稳定 SD 颗粒的浓度十分敏感。此外，χ_{ARM}的假设是，ARM 与直流偏转场线性相关，而这个假设在 DC 场>∽80 μT 才是基本成立的 [*Tauxe*, 1993]。ARM 强烈依赖于磁性颗粒浓度，但是由于磁性粒子之间的相互作用，ARM 也会随着浓度增加而减小 [*Sugiura*, 1979]。最后，ARM 的获得同时受设备差异、AF 和 DC 的大小、衰减速率[*Yu and Dunlop*, 2003]以及不同实验参数的影响[*Sagnotti et al*., 2003]。

当样品暴露于瞬间的（纳秒或毫秒）大磁场下时，它将沿着外场方向重磁化，这个剩磁即被称为等温剩磁（IRM）。IRM 随着外加场的增加而增加，直到饱和，

最后获得室温下的饱和 IRM（SIRM 或 M_{rs}）。通常使用的直流场大小为 1 T，但是这样的场并不会使反铁磁性矿物（赤铁矿、针铁矿）达到饱和，因此，通常将 1 T 磁场下获得的 IRM 称作 $IRM_{1\ T}$ 而不是作为 SIRM。更高的外加磁场（1.5-2 T）是最好的，但即使这样仍然无法完全饱和赤铁矿或针铁矿，其中针铁矿（不包括 Al 替代）甚至到 57 T 仍然无法饱和[*Rochette et al*., 2005]。

SIRM 可以在磁性颗粒尺寸和矿物学保持相对稳定时反映磁性矿物浓度。与 χ_{ARM}/χ_{ferri} 类似，χ_{ARM}/SIRM 也可以用来表征粒度变化 [*Peters and Dekkers*, 2003]。在某些情况下，χ_{ARM}/SIRM 要比 χ_{ARM}/χ_{ferri} 优越，因为前者只受永久磁化颗粒的影响（即那些稳定的 SD 颗粒和晶粒尺寸较大的颗粒），而 χ_{ARM}/χ_{ferri} 也受到 SP 颗粒的强烈影响。SIRM/χ 也常用作沉积环境中 SD 胶黄铁矿颗粒含量的指标[e.g., *Snowball*, 1991; *Roberts and Turner*, 1993; *Roberts*, 1995]，因为相对于 χ，SIRM 的增强表明了具有强磁记录能力的 SD 颗粒含量。

与剩磁一样，感磁（M）也随着外加磁场的增加而增加。在临界磁场（磁铁矿约 300 mT）时，电子自旋是完全一致，M 不再随着外场的增加而增加，此时所产生的感磁即饱和磁化强度（M_s）。与其它参数不同，M_s 不依赖于粒径大小，因此，它可以很好地表征磁性矿物浓度。因为 M 是有场测量，所以需要将顺磁性物质的磁化率（从高场斜率中估算）减去才能得到真实的测量结果。M_s 同样可以与其它参数进行综合表征，例如，χ_{ferri}/M_s 对 SP 颗粒的存在非常敏感[*Hunt et al*., 1995a; *Liu et al*., 2003]，因为 M_s 对 SP 颗粒的响应比 SD 颗粒强。

亚铁磁性矿物（磁铁矿、赤铁矿、磁铁矿、磁黄铁矿、胶黄铁矿）的磁化强度比反铁磁性矿物（赤铁矿和针铁矿）高出两个量级，因此这些弱磁性矿物的信号往往被强磁性矿物所掩盖 [e.g., *Liu et al*., 2002]。然而，它们的磁信号可以利用磁“硬度”（即矫顽力）进行不同程度的分离。热能或外部磁场可以提供克服磁矩沿易磁化轴的方向排列所需的能量。对于单个颗粒，从一个易磁化轴方向翻转到另一个易磁化轴方向所需的外加磁场大小称为微观矫顽力。在磁性矿物集合中，可以使磁化强度从饱和变为零的磁场大小称为矫顽力，用 H_c（单位 A/m）或 B_c（单位 T） 表示。

对于一个随机定向的赤铁矿颗粒分布，B_c 通常在 100-300 mT（针铁矿更高），而磁铁矿（磁赤铁矿）只有几十 mT。为了从磁铁矿（磁赤铁矿）中区分出赤铁

矿或针铁矿的矫顽力信号，可以利用“硬”的 IRM（HIRM）（HIRM = (SIRM + $IRM_{-0.3\ T}$)/2，其中 $IRM_{-0.3\ T}$ 是反向施加 300 mT 场后的 IRM）、S-ratio（S = (-$IRM_{-0.3T}$/SIRM) ）[*King and Channell*, 1991]。HIRM 可用来检测高矫顽力磁性矿物（如赤铁矿和针铁矿）的浓度，而 S-ratio 用来判断亚铁磁性矿物（如磁铁矿，磁赤铁矿）和高矫顽力矿物的相对丰度。当 S-ratio 接近 1 时，亚铁磁性矿物占主导地位。赤铁矿（针铁矿）的浓度增加， S-ratio 逐步降低。但 S-ratio 表征高低矫顽力矿物相对浓度的变化是非线性的，并且其解释也不唯一[e.g., *Heslop*, 2009]。*Liu et al*. [2007b] 提出 L-ratio = (SIRM + $IRM_{-0.3T}$)/(SIRM + $IRM_{-0.1T}$)) 来判断赤铁矿的硬度对 HIRM 和 S-ratio 的影响。只有当 L-ratio 稳定时，HIRM 和 S-ratio 才能按照传统解释。L-ratio 的变化表明了高矫顽力组分的粒径分布变化，这可能反映了源区变化或其他因素影响了赤铁矿和针铁矿的性质和相对含量 [*Liu et al.*, 2007b]。

文献速递

1. 末次冰期以来南大洋大象岛沿岸的古海洋研究：对海表生产力，营养盐利用率，底流和冰筏碎屑之间联系的指示

翻译人：仲义 zhongy@sustech.edu.cn

Sunghan Kim, Kyu-Cheul Yoo, Jae II Lee, et al.,* ***Paleoceanographic changes in the Southern Ocean off Elephant Island since the last glacial period: Links between surface water productivity, nutrient utilization, bottom water currents, and ice-rafted debris [J] Quaternary Science Reviews****, 2020, 106563.* https://doi.org/10.1016/j.quascirev.2020.106563

摘要：为了了解南极半岛周边南大洋中海洋与冰冻圈之间耦合关系，作者利用大象岛附近采集的三个沉积物岩心，多指标重建了末次冰期以来的古生产力、营养盐利用率、底流强度、和冰筏碎屑的变化。冰期表现为表层生产力降低，营养盐利用率升高，说明该时期的表层水的分层作用影响。而在冰消期以来，伴随营养盐利用率降低，表层生产力升高，而这种生产力的升高与次表层水的营养供应增加有关，由于气候变暖，锋面南移，绕南极环流（ACC）增强。在冰消期中大量粒径大于 1mm 的出现表明冰原迅速消退，大规模融化的崩解。然而在冰期时，粗粉砂-细砂粒级范围的出现表明该时期冰筏碎屑的大量出现。不同粒径范围冰筏碎屑（IRD）在不同时期出现被认为与 IRD 来源特征有关。不考虑 IRD 本身输入变化，可分选性粉砂的平均粒径和百分含量的相关系分析显示沉积物受到底流的分选作用影响。然而，他们的交叉图呈现出不同的时间关系。沉积物受到 ACC 和西南向底流的分选作用，而伴随着锋面和 ACC 的整体向南移动，西南向的底层流作用开始减弱，而 ACC 在 7 ka 开始增强。我们的结果表明斯科舍海的沉积过程大部分受到区域性海洋和冰盖圈层的交互作用影响。

ABSTRACT: To understand past changes in oceanecryosphere interactions in the Southern Ocean off the Antarctic Peninsula, multi-proxy analyses of three sediment cores located off Elephant Island were used to reconstruct changes in paleoproductivity, nutrient utilization, bottom current intensity, and iceberg calving since the last glacial period. The glacial period was characterized by low surface water productivity with high nutrient utilization, indicating surface water stratification. During the

deglaciation, surface water productivity increased with decreasing nutrient utilization, implying that the increase is associated with increased nutrient supply from the subsurface water by enhancing Antarctic Circumpolar Current (ACC) influence as fronts migrate southward with warming. Abundant occurrence of grains >1 mm during the deglacial period indicates rapid ice sheet retreat with large-scale melting and calving. During the glacial period, however, coarse siltefine sand-sized fraction represented ice-rafted debris (IRD). The different IRD grain size characteristics are thought to be related to the IRD source material characteristics. Regardless of IRD input, the running downcore correlation (5 to 9-point) between sortable silt mean grain size and percentage showed that sediments are well sorted by bottom current. However, the cross plot of them showed different temporal relationships. Sediments were sorted by the ACC and southwestward flowing bottom current. Along with southward migration of fronts and the ACC, southwestward flowing bottom current influence diminished, whereas the ACC influence increased particularly from 7 ka. Our results indicate that the sedimentary processes in the Scotia Sea largely depend on the regional interactions between the ocean and the cryosphere.

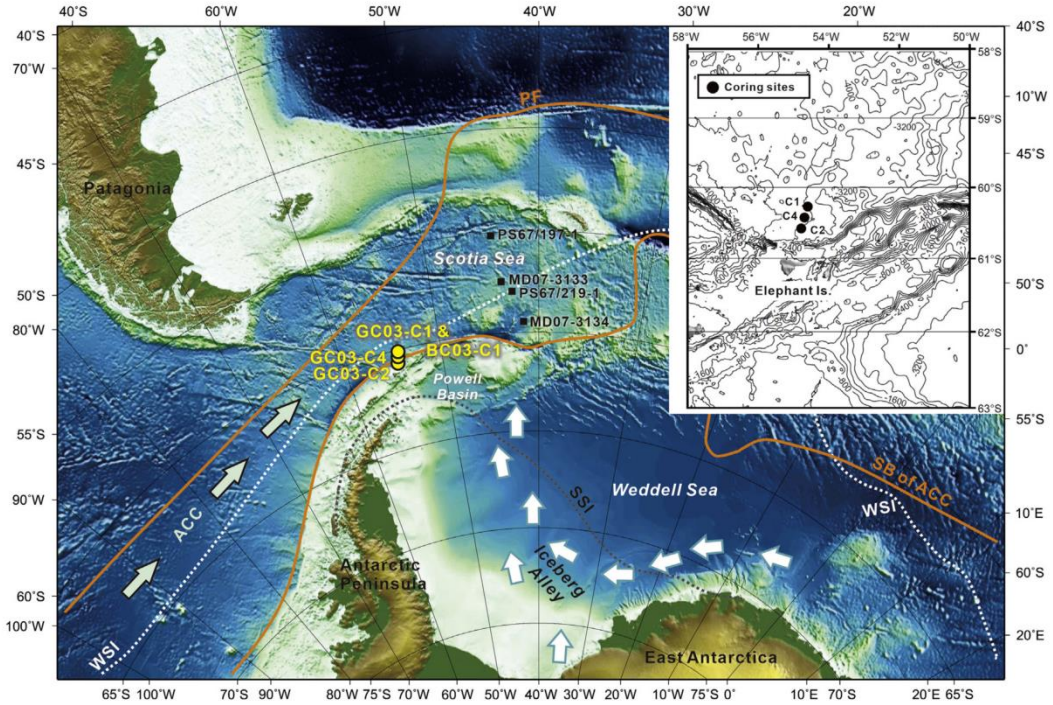

Figure 1. (a) Map of the study region indicating the locations of the sediment cores examined in this study as well as in previous investigations. The white open arrows indicate the location of iceberg alley (from Anderson and Andrew, 1999); the orange lines indicate the Polar Front (PF) and the Southern Boundary of the Antarctic Circumpolar Current (SBACC; Orsi et al., 1995); the dark gray and white dashed lines indicate the summer (SSI) and winter (WSI) sea ice extent, respectively (Gersonde et al., 2005); and the light green arrows indicate the ACC.

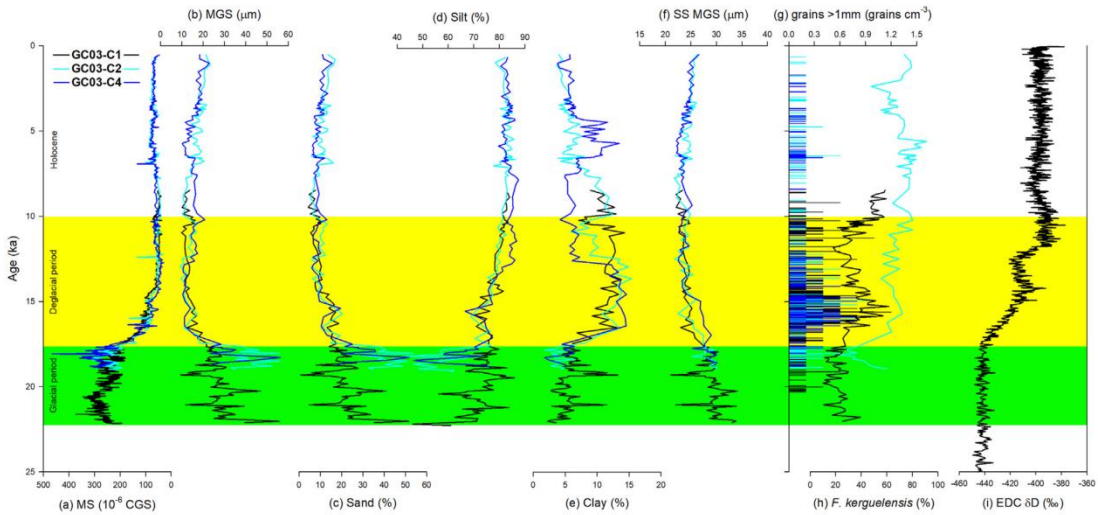

Figure 2. Downcore profiles of (a) MS, (b) mean grain size (MGS), (c) sand proportion, (d) silt proportion, (e) clay proportion, (f) sortable silt MGS, and (g) abundance of grains >1 mm per cm3 of cores GC03-C1 (black), -C2 (cyan), and -C4 (blue); (h) the relative abundance of open ocean diatom F. kerguelensis

in GC03-C1 (Bak et al., 2010) and GC03-C2 (Bak et al., 2014); and (i) the EDC dD ice core record (Jouzel et al., 2007).

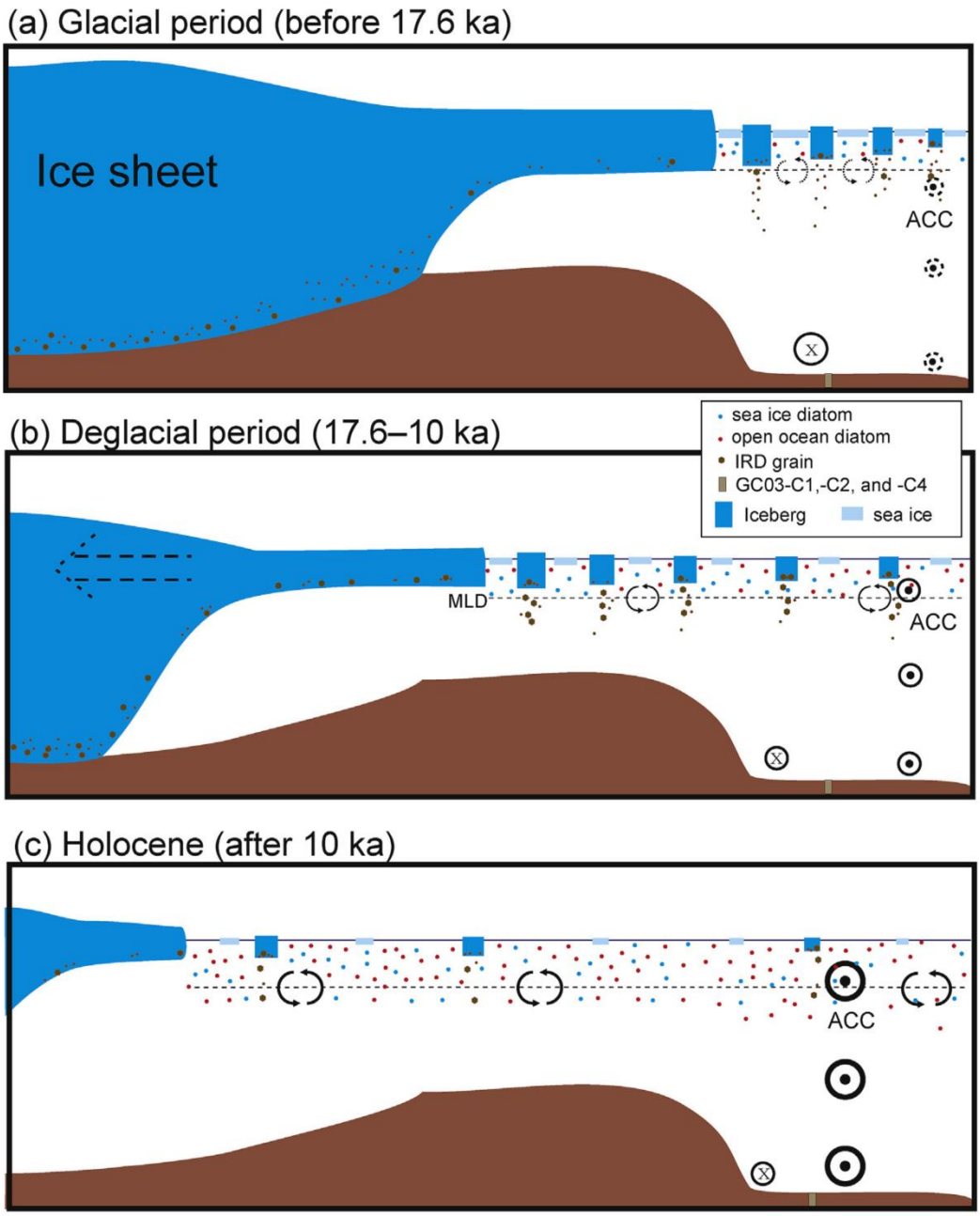

Figure 3. Paleoceanographic models of (a) the glacial period (before 17.6 ka), (b) the deglacial period (17.6e10 ka), and (c) the Holocene (after 10 ka) in the Southern Ocean off Elephant Island. MLD is the mixed layer depth.

2. 古新世-始新世边界温度与碳酸盐共同演化：来自印度洋低纬度微量元素新纪录

翻译人：蒋晓东 jiangxd@sustech.edu.cn

Barnet J S K, Harper D T, Levay L J, et al. ***Coupled evolution of temperature and carbonate chemistry during the Paleocene–Eocene; new trace element records from the low latitude Indian Ocean*** *[J].* ***Earth and Planetary Science Letters****, 2020, 545, 116414.*

https://doi.org/10.1016/j.epsl.2020.116414

摘要：早第三系早期近几个百万年的时期内代表了地球历史中最接近现今温室效应引起全球温度升高的情况。然而，对于低纬度尤其印度洋，长尺度气候和碳循环的理解仍然并不清楚。本研究第一次提供了长尺度亚偏心率分辨率的稳定同位素（$\delta^{13}C$ 和 $\delta^{18}O$）和微量元素记录，该记录横跨晚古新世-始新世（~58-53 Ma），以及北印度洋表层到深处的水道学重建，解析了晚古新世 405 kyr 的步调周期和一部分 PETM 的重建。我们的记录揭示水柱中各层位温度约 4-5 度的升高，且相较于低纬度太平洋表层温度更高。由于暖化的结果，我们发现混合层海水 $\delta^{18}O$ 长尺度的增加，暗示了增强的净蒸发。我们发现在~57-54 Ma 在混合层跃温层物种的崩塌，该结果可能是因为同质混合水层变厚或者 *Morozovella* 物种响应变暖时随深度的迁移。高低温度同步变暖，以及浮游有孔虫 B/Ca 的降低指示海洋 pH 的降低或者溶解无机碳的增加。结果表明这一时期全球气候是由上升的 CO_2 浓度驱动。

ABSTRACT: The early Paleogene represents the most recent interval in Earth's history characterized by global greenhouse warmth on multi-million year timescales, yet our understanding of long-term climate and carbon cycle evolution in the low latitudes, and in particular the Indian Ocean, remains very poorly constrained. Here we present the first long-term sub-eccentricity-resolution stable isotope ($\delta^{13}C$ and $\delta^{18}O$) and trace element (Mg/Ca and B/Ca) records spanning the late Paleocene–early Eocene ~58–53 Ma) across a surface–deep hydrographic reconstruction of the northern Indian Ocean, resolving late Paleocene 405-kyr paced cyclicity and a portion of the PETM recovery. Our new records reveal a long-term warming of ~4–5◦C at all depths in the water column, with absolute surface ocean temperatures and magnitudes of warming comparable to the low latitude Pacific. As a result of warming, we observe a long-term increase in $\delta^{18}O_{sw}$ of the mixed layer, implying an increase in net evaporation. We also observe a collapse in the temperature gradient between mixed layer-and thermocline-dwelling species from ∼57–54 Ma, potentially due to either the development of a more homogeneous water column with a thicker mixed layer, or depth migration of the Morozovellain response to warming. Synchronous warming at both low and high latitudes, along with decreasing B/Ca ratios in planktic foraminifera indicating a decrease in ocean pH and/or increasing dissolved inorganic carbon, suggest that global climate was forced by rising atmospheric CO^2 concentrations during this time.

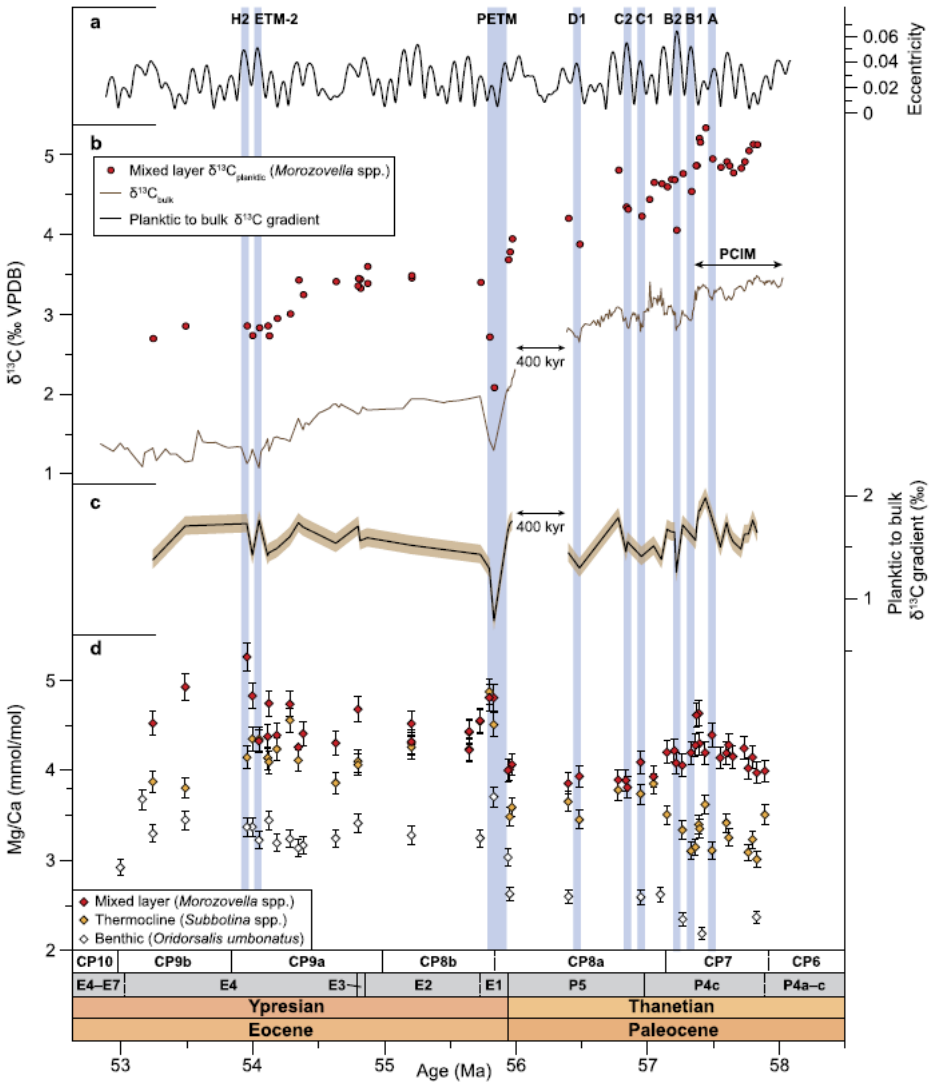

Figure 1. Raw Mg/Ca data for mixed layer, thermocline, and intermediate water depths plotted against age. (a) La2010b orbital solution (Laskar et al., 2011). (b) IODP Hole U1443A/ODP Hole 758A $\delta^{13}C_{bulk}$ and $\delta^{13}C_{plankt}$ records with latest Paleocene core gap indicated. PCIM =Paleocene Carbon Isotope Maximum. (c) Planktic to bulk $\delta^{13}C$ gradient with latest Paleocene core gap indicated. Pale brown shading represents uncertainty (±0.1), based on the analytical uncertainty on the$\delta^{13}C_{plankt}$ and $\delta^{13}C_{bulk}$ measurements. (d) Raw Mg/Ca data for the IODP Hole U1443A/ODP Hole 758A splice, color coded by genus/depth habitat. Error bars indicate analytical uncertainty on the Mg/Ca measurements (±3%). See Supplementary Figs. S1 and S2 for planktic $\delta^{13}C$ and Mg/Ca data plotted by foraminiferal species.

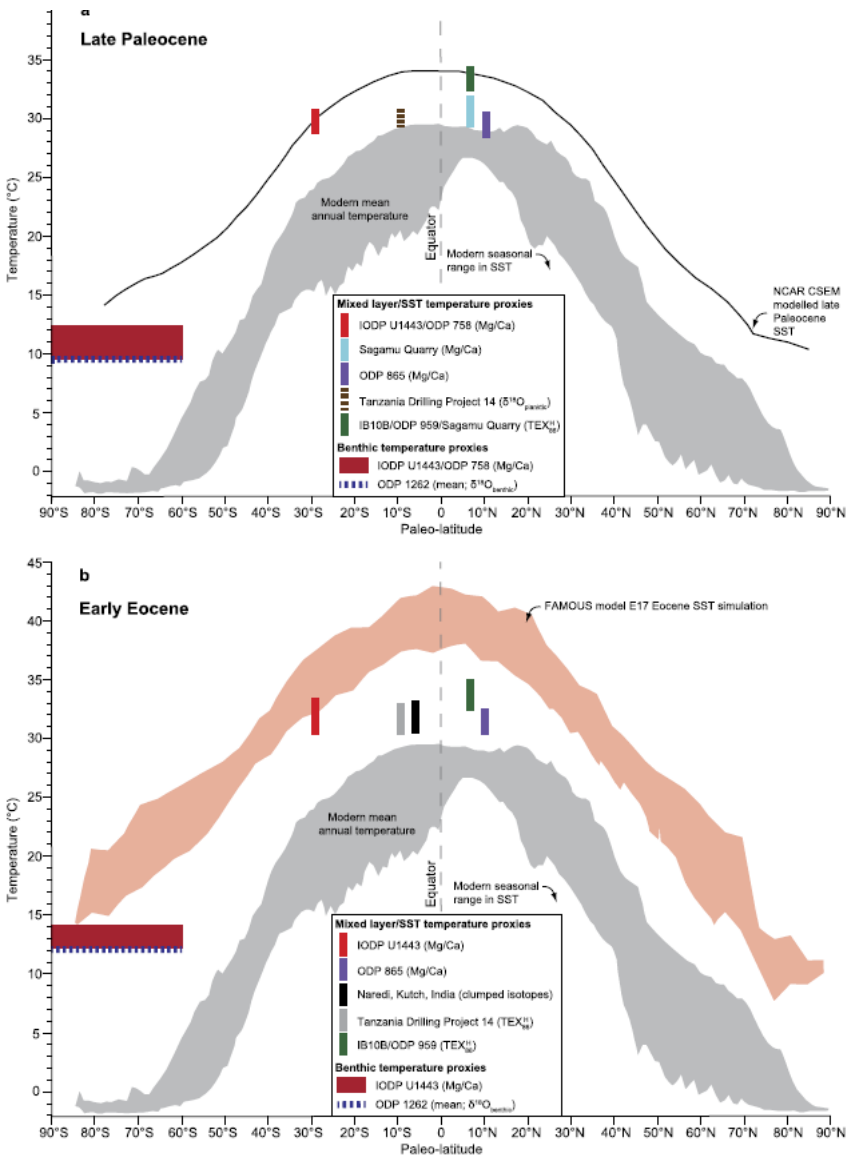

Figure 2. Comparison between proxy data and modelingresults for late Paleocene–early Eocene sea surface temperature (SST), with modern mean annual temperature and seasonal range in SST also shown for comparison (Locarnini et al., 2013). (a) Late Paleocene temperature proxy data plotted against the modeledmeridional SST gradient based on the National Center for Atmospheric Research Community Earth System Model (NCAR CESM1) from Frieling et al. (2017), assuming a radiative forcing equivalent to 2240 ppm CO_2. (b) Early Eocene temperature proxy data plotted against the modeledmeridional SST gradient based on the FAMOUS Model E17 Eocene simulation from Sagoo et al. (2013), assuming a radiative forcing equivalent to 560 ppm CO_2. All low latitude surface ocean and benthic IODP Site U1443/ODP Site 758 temperature proxy data are plotted as ranges of values for the late Paleocene and early Eocene in (a) and (b) respectively, while mean late Paleocene and early Eocene temperatures are plotted for ODP Site 1262. PETM proxy data are considered anomalous and have been excluded. Paleo-

latitudes for the low latitude sites were computed relative to the paleomagnetic reference frame of Torsvik et al. (2012), using Version 2.1 of the model from paleolatitude.org (Van Hinsbergen et al., 2015). Benthic temperature proxy data from IODP Site U1443/ODP Site 758 (∼1500 m paleo-depth) and ODP Site 1262 (∼3500 m paleo-depth) are interpreted as crude estimates for high southern latitude SSTs at >60◦S, as early Paleogene deep waters in the South Atlantic and Indian oceans were predominantly formed in the Southern Ocean. See Fig.1for site locations and Supplementary Table S2 for the sources of all published data. All published Mg/Ca temperature estimates included in this figure were recalibrated following the Hollis et al. (2019)approach used in this study. However, temperature estimates based on other proxies remain unchanged from the original literature source. All TEX86temperatures are plotted using the TEXH86calibration (Kim et al., 2010).

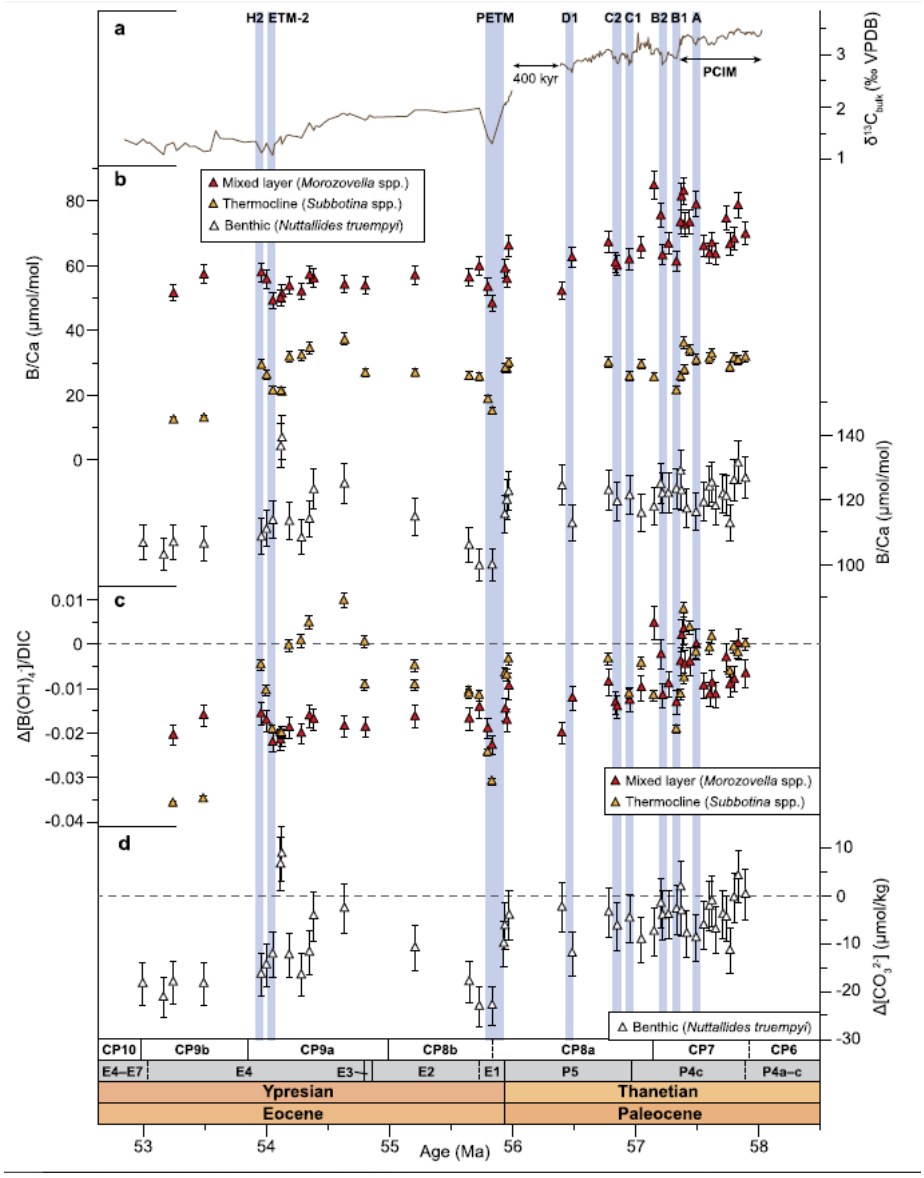

Figure 3. Raw B/Ca data and carbonate chemistry for mixed layer, thermocline, and intermediate water depths plotted against age. (a) IODP Hole U1443A/ODP Hole 758A $\delta^{13}C_{bulk}$ record, with latest Paleocene core gap indicated. PCIM =Paleocene Carbon Isotope Maximum. (b) Raw B/Ca data for the IODP Hole U1443A/ODP Hole 758A splice, color-coded by depth habitat. Error bars indicate analytical uncertainty on the B/Ca measurements (±5%). (c) Change in mixed layer and thermocline carbonate chemistry (borate ion/dissolved inorganic carbon ratio; $\triangle[B(OH)_4]/DIC$), plotted as the change relative to a baseline of 0 for peak PCIM conditions. (d) Change in benthic (intermediate water depth) carbonate chemistry (carbonate ion concentration; $[CO_3^{2-}]$), plotted as the change relative to a base line of 0 for peak PCIM conditions. Error bars on the carbonate chemistry data points indicate propagated analytical uncertainties associated with the B/Ca data points.

3. 超深金刚石记录了岩石圈至下地幔的碳循环过程

翻译人：冯婉仪 fengwy@sustech.edu.cn

Regier M E,Pearson D G, Stachel T, et al. ***The lithospheric-to-lower-mantle carbon cycle recorded in superdeep diamonds****[J].* ***Nature****, 2020, 585: 234-238.*

https://doi.org/10.1038/s41586-020-2676-z

摘要：碳进入地幔是地球碳循环的重要途径，影响着气候以及地表和地幔的氧化还原条件。在这个循环中，没有被约束的最大变量是沉积物和蚀变洋壳中的碳可以俯冲到什么深度，以及这些储库对地幔深部中碳存储的相对贡献。岩石圈之下或“超深”金刚石（来自于 250 公里以上的深度）中的矿物包裹体可以用来约束这些变量。在这里，我们展示了来自几内亚坎坎的岩石圈至下地幔不同深度（超过 660 公里）的金刚石中的矿物包裹体的氧同位素测量数据。这些数据以及金刚石的碳和氮同位素组成，表明在俯冲到岩石圈深部和过渡带深处（小于 660 公里）的板片中，主要的含碳储库不是沉积物，而是碳酸盐化的火成洋壳。在这个深度范围内，岩石圈地幔之下的包裹体相对于从地壳原岩中衍生出来的榴辉岩相岩石圈包裹体更加富集 ^{18}O。这些岩石圈地幔之下的包裹体 ^{18}O 含量的增加是由于它们是从富含碳酸盐的俯冲洋壳熔融所形成的熔体中结晶而成。相比之下，下地幔矿物包裹体及其宿主金刚石（深度超过 660 公里）的同位素值变化范围很小，这是几乎没有经历与地壳相互作用的地幔的典型特征。由于碳赋存在金属中，而不是金刚石中，在还原的、贫挥发组分的下地幔中，碳必须被迁移和富集以形成下地幔中的金刚石。我们的数据支持了一个模型，即俯冲的大洋岩石圈使下地幔的最上层水化，使含碳金属不稳定，从而形成金刚石，在这个过程中没有干扰周围地幔的稳定同位素特征。这种从过渡带碳酸盐化板片融化到下地幔板片脱水的转变支持了下地幔是碳俯冲的屏障的观点。

ABSTRACT: The transport of carbon into Earth’s mantle is a critical pathway in Earth’s carbon cycle, affecting both the climate and the redox conditions of the surface and mantle. The largest unconstrained variables in this cycle are the depths to which carbon in sediments and altered oceanic crust can be subducted and the relative contributions of these reservoirs to the sequestration of carbon in the deep mantle. Mineral inclusions in sublithospheric, or “superdeep”, diamonds (derived from depths greater than 250 kilometres) can be used to constrain these variables. Here we present oxygen isotope measurements of mineral inclusions within diamonds from Kankan, Guinea that are derived from depths extending from the lithosphere to the lower mantle (greater than 660 kilometres). These data, combined with the carbon and nitrogen isotope contents of the diamonds, indicate that carbonated igneous oceanic crust, not sediment, is the primary carbon-bearing reservoir in slabs subducted to deep-lithospheric and transition-zone depths (less than 660 kilometres). Within this depth regime, sublithospheric inclusions are distinctly enriched in ^{18}O relative to eclogitic lithospheric inclusions derived from crustal protoliths. The increased ^{18}O content of these sublithospheric inclusions results from their crystallization from melts of carbonate-rich subducted oceanic crust. In contrast, lower-mantle mineral inclusions and their host diamonds (deeper than 660 kilometres) have a narrow range of isotopic values that are typical of mantle that has experienced little or no crustal interaction. Because carbon is hosted in metals, rather than in

diamond, in the reduced, volatile-poor lower mantle, carbon must be mobilized and concentrated to form lower-mantle diamonds. Our data support a model in which the hydration of the uppermost lower mantle by subducted oceanic lithosphere destabilizes carbon-bearing metals to form diamond, without disturbing the ambient-mantle stable-isotope signatures. This transition from carbonate slab melting in the transition zone to slab dehydration in the lower mantle supports a lower-mantle barrier for carbon subduction.

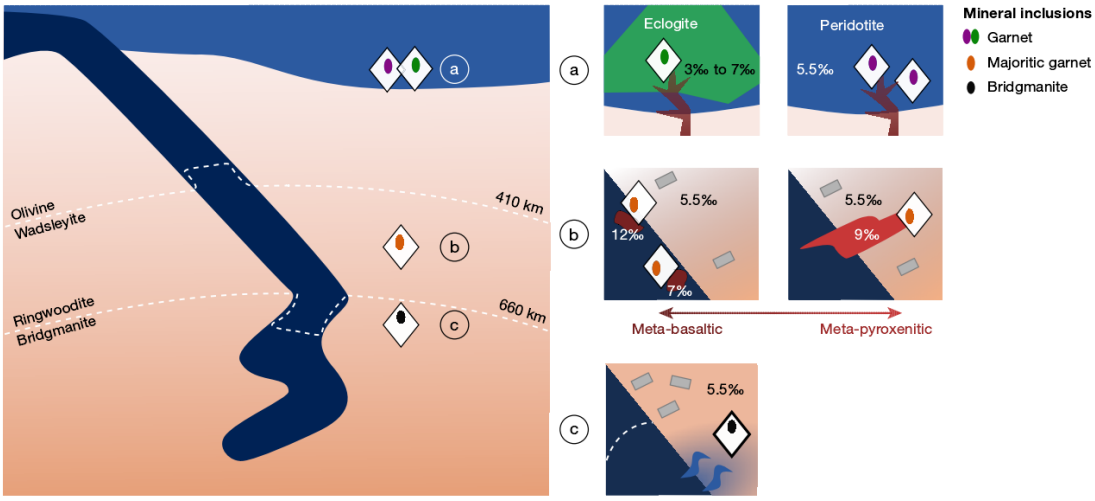

Figure 1. Model of diamond formation in the lithosphere, transition zone and lower mantle. a, Lithospheric diamond forms by fluid or melt metasomatism of eclogitic and peridotitic substrates[43], but the $\delta^{18}O$ value of the inclusions is buffered by the host lithology[20]. b, In the transition zone, the carbonate-rich upper portion of a subducting slab produces carbonatitic melt. Diamonds and majoritic garnet inclusions crystallize during the interaction of the carbonatitic melt with reduced, metal-bearing convecting mantle. The short melt migration path and the limited interaction with convecting mantle produces majoritic garnet with eclogitic compositions and elevated $\delta^{18}O$, directly reflecting the local carbonated AOC melt source. Greater levels of interaction with the convecting mantle are reflected in the lower $\delta^{18}O$ and increasingly ultrabasic, meta-pyroxenitic character of some majorites. c, As the slab penetrates into the lower mantle, the negative pressure–temperature slope (the Clapeyron slope) of the post-spinel transition[44] and the delayed garnet-to-perovskite transition in metabasaltic lithologies[45] retards the formation of lower-mantle minerals (dotted white line). The transition to a lower-mantle mineralogy leads to slab dehydration and the hydration of the surrounding mantle. The hydrated ambient mantle releases carbon from its metallic iron hosts to form diamond.

4. Futuna 岛东南部广泛分布的火山：近海底磁异常定年和区域性的结果

翻译人:李园洁 liyj3@sustech.edu.cn

Szitkar F, Dyment J, Fouquet Y. ***Widespread volcanism Southeast of Futuna Island (SW Pacific Ocean): Near-seafloor magnetic dating and regional consequences[J]. Journal of Volcanology and Geothermal Research****, 2020: 107064. https://doi.org/10.1016/j.jvolgeores.2020.107064*

摘要：本文对西南太平洋的 Futuna 岛的东南部火山活跃区域利用自主水下航行器（AUV）和载人潜水器（DSS）进行近海底测深和磁测。这个区域位于太平洋板块和澳大利亚板块交会处的劳盆地和北斐济海盆边缘，主要特征是强烈的火山和构造活动。潜水器直接观测结果表明海底由最新的岩浆流，火山，充满岩浆流的活跃或不活跃的火山口以及热液口覆盖。作者综合 AUV 网格化磁测数据的 Bayesian 反演结果和潜水器数据的反演结果估计出岩石磁极性和绝对磁化强度来研究火山的年代。作者发现一些火山在最近一个地磁极性倒转（780kyr）之前存在，而其周围表现出正极性，可能是最近喷发。这个结果表明这个区域的海底在过去几个百万年经历了连续和不连续的火山活动。

ABSTRACT：Near-seafloor bathymetric and magnetic data have been collected by Autonomous Underwater Vehicle (AUV) and manned submersible (DSS) over a volcanically active area southeast of Futuna Island, French Territory of Wallis-and-Futuna, in the Southwestern Pacific Ocean. Located at the edge of the Lau and North Fiji basins, at the convergence of the Pacific and Australian plates, this area is characterized by intense volcanic and tectonic activity. Direct observation by submersible reveals that the seafloor is covered by recent lava flows, volcanoes and large, active or inactive calderas filled by smooth lava flows and eventually hosting hydrothermal sites. We investigate the volcanic chronology by combining a Bayesian inversion of the AUV-gridded magnetic data with an inversion of the submersible data specifically designed to estimate the rock magnetic polarity and absolute magnetization. We show that some volcanoes predate the last (Brunhes-Matuyama) magnetic polarity reversal 780 kyr ago whereas their neighbors exhibit a normal polarity and appear to be recent. This result suggests that the seafloor in this region has undergone continuous and sparse volcanic activity over the last few million years.

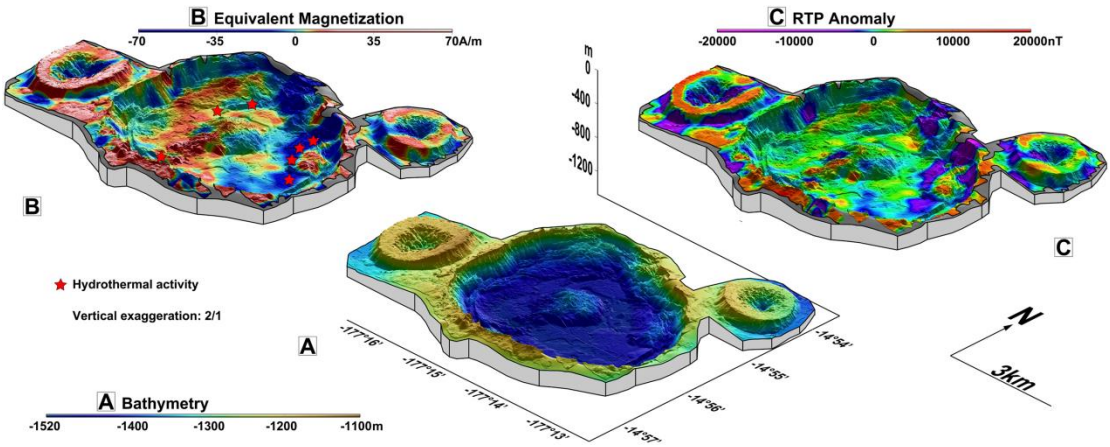

Figure 1. (A) High-resolution bathymetry of the Kulo Lasi Caldera. The smooth bathymetry at its bottom corresponds to new and mostly basaltic lava flows with some andesitic flows. (B) Equivalent magnetization derived from the AUV magnetic anomalies using Honsho’s Bayesian inversion (2012). (C) Reduced-to-the-Pole magnetic anomaly computed from the equivalent magnetization. The bottom of the caldera is associated with a relatively weak magnetic anomaly by comparison with the top of the two flanking volcanoes. To the Northeast, an elongated negative magnetic anomaly corresponds to a hydrothermally active area, in accordance with previous studies in basaltic (e.g., Tivey et al, 1993) and andesitic (Fujii et al, 2015) contexts.

5. 2005 年至 2010 年南部非洲南大西洋异常的演变：基于地面和卫星数据的谐波样条磁场主磁场模型

翻译人：柳加波 liujiabo7@gmail.com

Nahayo E, Kotzé P B, Korte M, et al. ***A harmonic spline magnetic main field model for Southern Africa combining ground and satellite data to describe the evolution of the South Atlantic Anomaly in this region between 2005 and 2010****[J].* ***Earth, Planets and Space****, 2018, 70(1): 30*
https://doi.org/10.1186/s40623-018-0796-6

摘要：CHAMP 卫星和 2005 年至 2010 年间在南部非洲测得的相对密集的地面数据被整合到一个新区域的、基于谐波样条方法的、核心场模型中。这个新的 SACFM-2 模型用来和仅基于卫星数据的 SARM 区域模型，以及 CHAOS-6 全球模型进行对比。结果表明，他们在垂直（Z）分量中非常吻合，在水平分量中差异较大。Z 分量和总强度 F 用于研究该区域南大西洋异常的演变。在研究时间范围内，计算的 Z 分量和总强度 F 的主磁场分布显示，地磁场在该区不断衰减。这指示了南部非洲南大西洋异常的演变，并且在该区域不断增强。

ABSTRACT: CHAMP satellite and relatively densely spaced ground-based data measured over southern Africa between 2005 and 2010 are combined in a new regional, harmonic spline based, core field model. This new SACFM-2 model is compared to the regional SARM model, which is based only on satellite data, and the global CHAOS-6 model. The results agree well in the vertical (Z) component, with somewhat larger differences in the horizontal components. The Z component and total intensity F are used to investigate the evolution of the South Atlantic Anomaly in this region. The computed maps of main field of the Z component and total intensity F show a steady decrease in the field over the years during the study period, indicating the evolution of the South Atlantic Anomaly over southern Africa and suggesting an increase in the area of this feature.

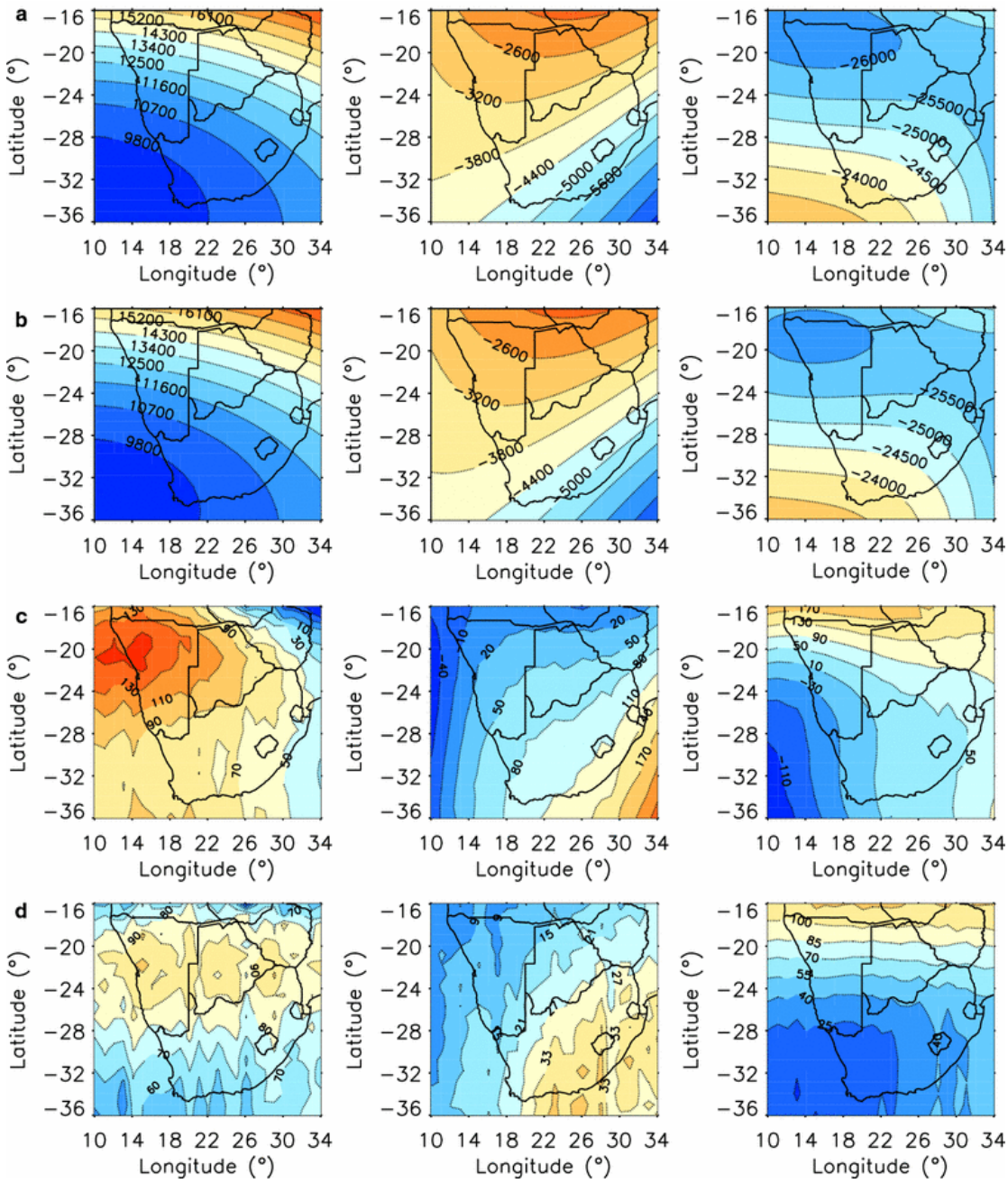

Fig 1: Comparison between SACFM-2 and CHAOS-6 at 2008.0 for 3 components X, Y and Z. Comparison of models SACFM-2 a and CHAOS-6 b at epoch 2008.0, their differences are shown in the third row c and last row d at 0.8 and 350 km altitudes, respectively. The three components X, Y and Z are plotted in the first, second and third columns, respectively. The unit is nanotesla

6. 新几内亚西北部新生代岩浆活动和碰撞历史为澳大利亚板块最北缘的构造演化提供了新的视角

翻译人：刘伟 inewway@163.com

Webb M, White L T, Jost B M, et al. The history of Cenozoic magmatism and collision in NW New Guinea–New insights into the tectonic evolution of the northernmost margin of the Australian Plate[J]. Gondwana Research, 2020, 82: 12-38.
https://doi.org/10.1016/j.gr.2019.12.010

摘要：沿新几内亚的走向方向发现了新生代岩浆活动的证据。然而这种岩浆作用的岩石学成因和构造背景却知之甚少。本研究基于新几内亚西北部新的野外、岩石学、U-Pb 锆石和地球化学资料，确定了记录渐新世、中新世和上新世岩浆作用的 6 个新生代火成岩单元。这些事件的发生是对澳大利亚板块和菲律宾海板块持续相互作用的响应。始新世期间，澳大利亚板块开始在菲律宾海板块下倾斜俯冲，形成菲律宾-卡洛琳弧。该弧的岩浆作用记录在新几内亚西北部的 Dore、Mandi 和 Arfak 火山中，这些火山在与俯冲相关的弧前和与伸展相关的弧后环境中于 32-27Ma 形成钙碱性岩和拉斑岩。渐新世--中新世板块边界的碰撞卡住了俯冲带，使俯冲极性由北倾向南倾反转。在此之后，菲律宾海板块俯冲到澳大利亚板块之下，在整个新几内亚西部产生了岩浆活动。在新几内亚的西北部，中中新世(18-12 Ma)的 Moon 火山活动记录了这一现象，其中包括早期的高钾—玄武质火山活动。这些早期的岩浆岩与俯冲带极性反转和一开始较陡的俯冲角度有关。岩浆活动后来转变为钙碱性成分，侵位成原始大陆弧前段的火山岩。最后，在晚中新世-上新世的弧-陆碰撞之后，地幔衍生的岩浆(包括 Berangan 安山岩)沿着大的走滑断层迁移，并在上新世-更新世喷发前被地壳混染。对新几内亚西北部新生代岩浆史的研究，为研究澳大利亚板块北缘的构造演化提供了新的资料和见解。

ABSTRACT: Evidence of Cenozoic magmatism is found along the length of New Guinea. However, the petrogenetic and tectonic setting for this magmatism is poorly understood. This study presents new field, petrographic, U–Pb zircon, and geochemical data from NW New Guinea. These data have been used to identify six units of Cenozoic igneous rocks which record episodes of magmatism during the Oligocene, Miocene, and Pliocene. These episodes occurred in response to the ongoing interaction between the Australian and Philippine Sea plates. During the Eocene, the Australian Plate began to obliquely subduct beneath the Philippine Sea Plate forming the

Philippine–Caroline Arc. Magmatism in this arc is recorded in the Dore, Mandi, and Arfak volcanics of NW New Guinea where calc-alkaline and tholeiitic rocks formed within subduction-related fore-arc and extension-related back-arc settings from 32 to 27 Ma. Collision along this plate boundary in the Oligocene–Miocene jammed the subduction zone and caused a reversal in subduction polarity from north-dipping to south-dipping. Following this, subduction of the Philippine Sea Plate beneath the Australian Plate produced magmatism throughout western New Guinea. In NW New Guinea this is recorded by the middle Miocene (18–12 Ma) Moon Volcanics, which include an early period of high-K to shoshonitic igneous activity. These earlier magmatic rocks are associated with the subduction zone polarity reversal and an initially steeply dipping slab. The magmatic products later changed to more calc-alkaline compositions and were emplaced as volcanic rocks in the fore-arc section of a primitive continental arc. Finally, following terminal arc–continent collision in the late Miocene–Pliocene, mantle derived magmas (including the Berangan Andesite) migrated up large strike-slip faults becoming crustally contaminated prior to their eruption during the Plio–Pleistocene. This study of the Cenozoic magmatic history of NW New Guinea provides new data and insights into the tectonic evolution of the northern margin of the Australian Plate.

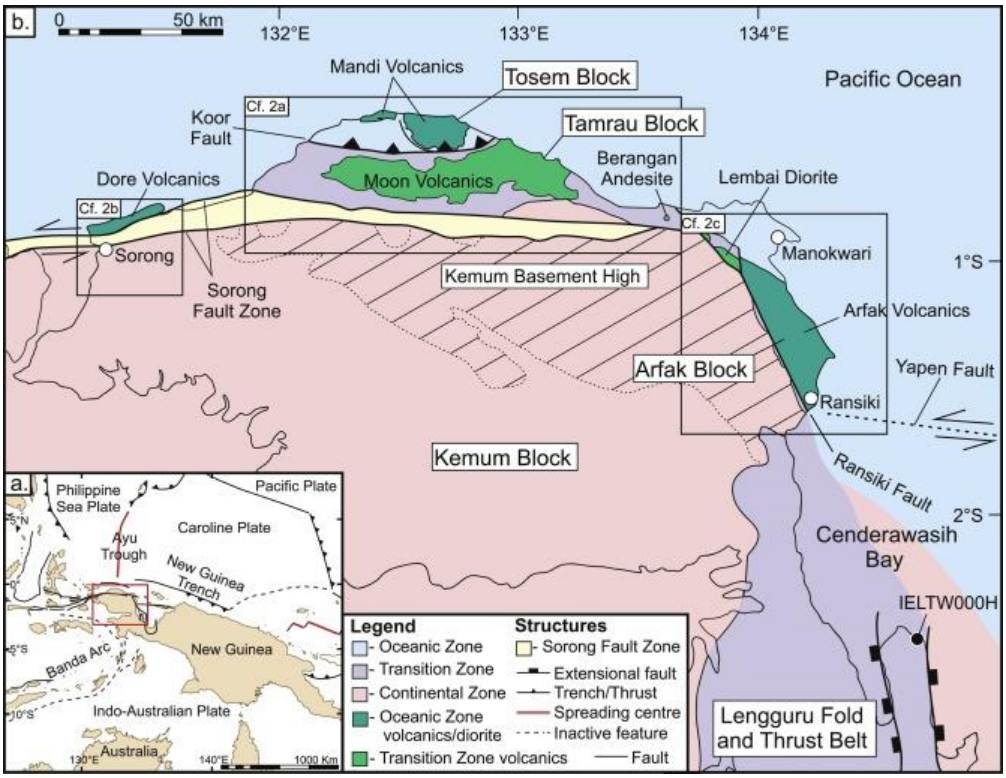

Figure 1. Location and overview geological maps of NW New Guinea.

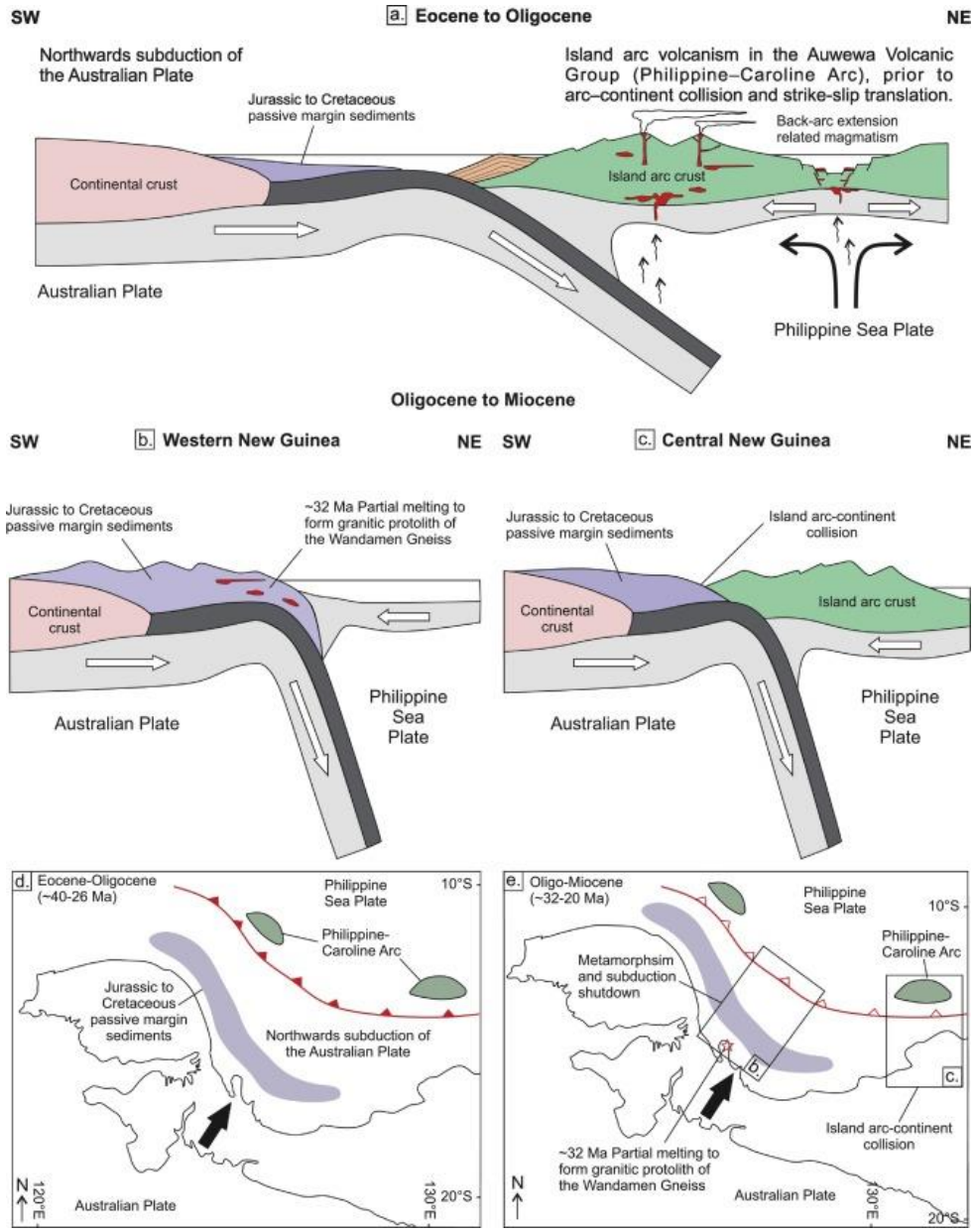

Figure 2. Cross-sectional and map-view tectonic models for NW New Guinea for the Eocene to Oligocene and the Oligocene to Miocene. a) The top panel depicts the Eocene to Oligocene northwards subduction of the Australian Plate beneath the Philippine Sea Plate and the formation of the Auwewa Volcanic Group of this study within the larger Philippine–Caroline Arc. b) The left-hand middle panel shows the Oligocene to Miocene collisional event described in this study and how it occurred in western New Guinea. Here Jurassic to Cretaceous passive margin sediments overlying Australian continental crust enter the north-dipping subduction zone and jam the system, this results in partial melting and formation of the granitic protolith in the Wandamen Gneiss. c) Oligocene to Miocene collisional event in central and eastern New Guinea. Here fragments of the Philippine–Caroline Arc collide with Australian continental crust and obduct along the northern margin of New Guinea. d) Map-view tectonic setting for the Eocene to Oligocene corresponding to (a). e) Map-view tectonic setting for the Oligocene to Miocene, geographic locations for (b) & (c) are displayed here. The map-view tectonic reconstructions are modified from Webb et al. (2019), palaeo-latitudes and longitudes and plate motions not referenced in the figure are derived from Hall, 2002, Hall, 2012.

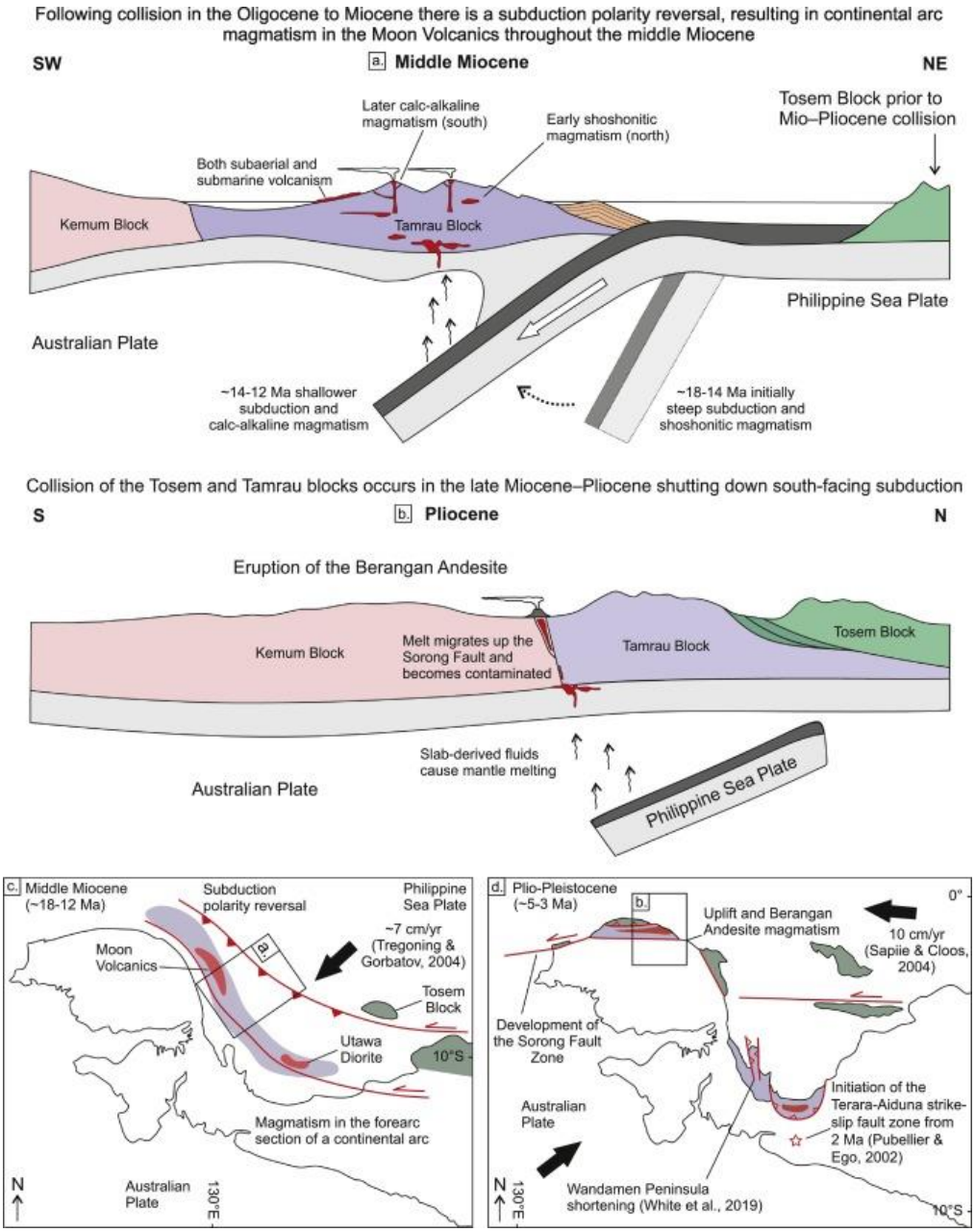

Figure 3. Cross-sectional and map-view tectonic models for NW New Guinea for the middle Miocene and Pliocene. a) The top panel depicts the middle Miocene southwards subduction of the Philippine Sea Plate beneath the Australian Plate and the Tamrau Block during the middle Miocene, this followed initial differential collision across New Guinea (Fig. 16) and a switch in the polarity of subduction. Subduction is initially steep, leading to shoshonitic magmatism from ~18–14 Ma in the northern Moon Volcanics, before shallowing and producing calc-alkaline magmatism from ~14–12 Ma in the south. b) The middle panel shows the Pliocene tectono-stratigraphic configuration of the Bird's Head Peninsula following late Miocene to Pliocene collision of the Tosem Block and the onset of Plio-Pleistocene magmatism in the Berangan Andesite. c) Map-view tectonic setting for the middle Miocene corresponding to (a). e) Map-view tectonic setting for the Plio-Pleistocene corresponding to (b). The map-view tectonic reconstructions are modified from Webb et al. (2019), palaeo-latitudes and longitudes and plate motions not referenced in the figure are derived from Hall, 2002, Hall, 2012.

7. 古地磁约束 Nuna 超大陆核心澳大利亚-劳伦古陆连接的持续时间

翻译人：曹伟 11930854@QQ.com

Kirscher U., Mitchell R.N., Liu Y.B., et al., ***Paleomagnetic constraints on the duration of the Australia-Laurentia connection in the core of the Nuna supercontinent****. [J].* ***Geology****, 2020(49)*
https://doi.org/10.1130/G47823.1

摘要：古元古代至中元古代 Nuna 超大陆中的澳大利亚-劳伦古陆连接被认为是在约 1.6Ga 开始的，当时两个大陆都被锁定在原始的 SWEAT(southwestern U.S. East Antarctic)构造中。然而这种结构的时限并没有良好的约束。本研究中我们展示了一个来自澳大利亚北部大约 1.3Ga Derim 基岩所指示的新的高质量古地磁极，它表明澳大利亚和劳伦古陆在当时处于相同的组构。这一新的古地磁极也支持了澳大利亚和华北之间的联系，并结合先前发表的来自各大洲的数据，表明 Nuna 大陆的解体主要发生在约 1.3 到 1.2 Ga 之间。

ABSTRACT: The Australia-Laurentia connection in the Paleoproterozoic to Mesoproterozoic supercontinent Nuna is thought to have initiated by ca. 1.6 Ga when both continents were locked in a proto-SWEAT (southwestern U.S. East Antarctic) configuration. However, the longevity of that configuration is poorly constrained. Here, we present a new high-quality paleomagnetic pole from the ca. 1.3 Ga Derim Derim sills of northern Australia that suggests Australia and Laurentia were in the same configuration at that time. This new paleopole also supports a connection between Australia and North China and, in conjunction with previously reported data from all continents, indicates that the breakup of Nuna largely occurred between ca. 1.3 and 1.2 Ga.

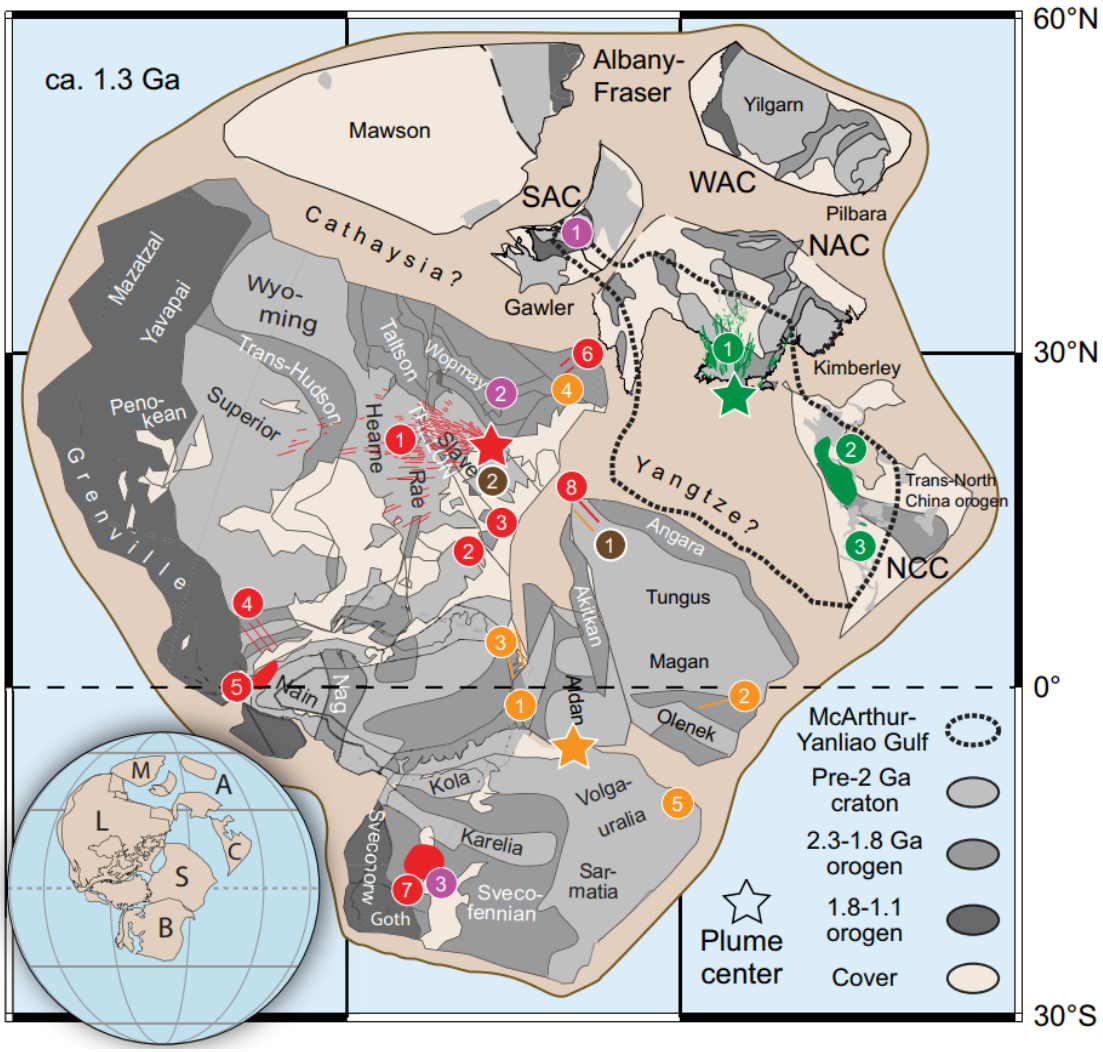

Figure 1. Paleogeography of Nuna at ca. 1.3 Ga including its core constituents Laurentia (L), Baltica (B), Siberia (S), Australia (A, including Mawson, M), and North China Craton (C). Main orogens are indicated. Large igneous provinces (LIPs) emplaced during Nuna breakup are also shown with associated dike swarms (lines) and proposed plume centers color-coded by age (stars; Table S6 [see footnote 1]). See Table S7 for Euler rotations. McArthur-Yanliao Gulf is outlined (Collins et al., 2019), also known as the Gulf of Nuna (Mitchell et al., 2020). NAC North Australia craton; NCC North China craton; SAC, South Australia craton; WAC, West Australia craton.

8. 晚第四纪东亚非均质降雨变化对哈德利环流重组的响应

翻译人：杨会会 11849590@mail.sustech.edu.cn

Zhao D B, Wan S M, Lu Z Y et al., ***Response of heterogeneous rainfall variability in East Asia to Hadley circulation reorganization during the late Quaternary [J].Quaternary Science Reviews****, 2020,247, 106562. https://doi.org/10.1016/j.quascirev.2020.106562*

摘要：利用中国洞穴石笋 $\delta^{18}O$ 记录重建的第四纪东亚夏季降水演化，在整个东亚地区具有一致性，长期以来被认为揭示了季风强度变化。季风强度的变化和全球气候的遥相关关系通常被认为由热带辐合带(ITCZ)的经向移动所导致。然而，许多其他指标记录、气候模拟和气象观测表明，东亚不同地区在多个时间尺度上的降雨模式不一致。这些东亚第四纪夏季降水的空间异质性表明，该地区的水文气候并没有完全受 ITCZ 迁移的影响。本文中,我们报告了一个揭示东海北部过去 400ka 降雨演化的沉积物记录。将该记录与瞬态气候模型模拟相结合,表明在岁差频率上东亚地区的中-东南部，北部和西南部地区的降雨具有反相关系，即当北半球夏季日照较高时，东亚地区的北部和西南部降雨强度增加，而东亚中部的降雨强度降低。我们将东亚降雨的区域异质性归因于响应半球经向温度梯度变化的哈德利环流重组，包括上升分支(ITCZ)和下降分支(副热带西风急流)的迁移。我们的研究结果强调了哈德利环流在东亚水文气候中的重要作用，并对未来的气候预测具有重要意义。

Abstract: The Quaternary East Asian summer rainfall evolution reconstructed with the Chinese speleothem $\delta^{18}O$ records shows the consistency throughout the region of East Asia, and has long been considered equivalent to the monsoon intensity. Its variation and teleconnection with global climate were usually interpreted by the meridional shift of the intertropical convergence zone (ITCZ). However, many other proxy records, climate simulations and meteorological observations suggest the inconsistent rainfall patterns in the different regions of East Asia on multi-timescales. Such spatial heterogeneity in Quaternary East Asian summer rainfall indicates that the hydroclimate in this region is not fully paced by the migration of the ITCZ. Here, we report a sediment record of rainfall evolution during the last 400 ka in the northern East China Sea, and this record, in combination with a transient climate model simulation, indicates an out-of-phase relationship between rainfall over middle-southeastern East Asia and northern and southwestern East Asia on the precession band, with high boreal summer insolation corresponding to the increased rainfall intensity in the northern and southwestern East Asia, however, decreased rainfall intensity in the middle East Asia. We attribute this regional heterogeneity in East Asian rainfall to the reorganization of the Hadley circulation, including shifts in the ascending branch (ITCZ) and descending branch (subtropical westerly jet), in response to changes in the hemispheric meridional temperature gradient. Our results highlight the crucial role of the Hadley circulation in the East Asian hydroclimate and have important implications for future climate projections.

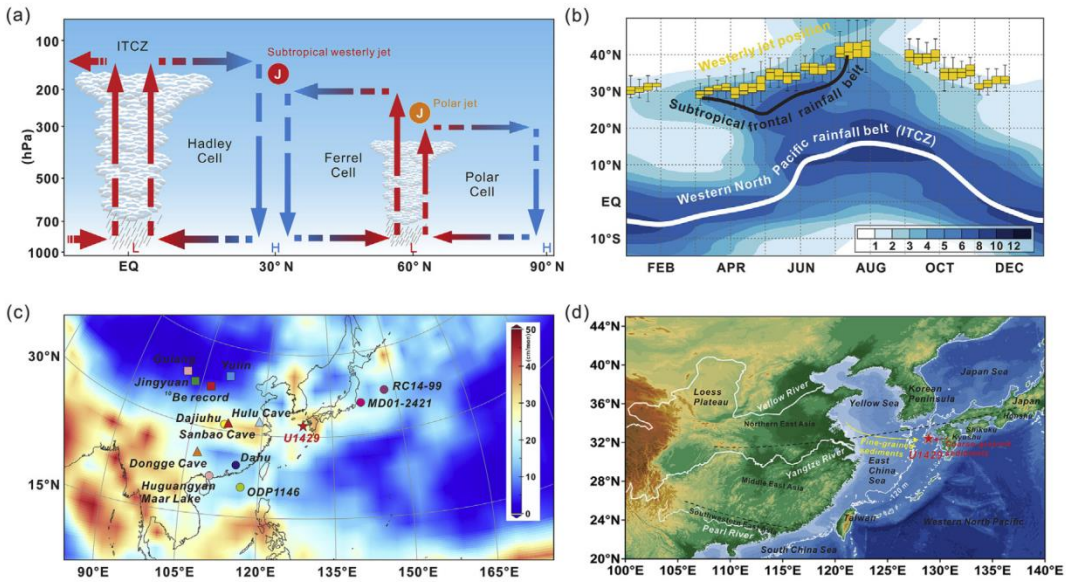

Figure 1. (a) Cross section of the Hadley Circulation and westerly jet as well as other atmospheric elements in the Northern Hemisphere. (b) Monthly mean rainfall as a function of latitude (ordinate) and calendar month (abscissa) (modified from Liu et al. (2008)). The precipitation is averaged over the East Asia sector between 110E and 130E. The black and white lines highlight the ITCZ and subtropical frontal rain belt, respectively. The yellow box plots indicate the interannual variability of East Asian westerly jet latitude between 110E and 130E (Schiemann et al., 2009), suggesting the coherency between the subtropical rainfall belt and the position of westerly jet from the early spring to late summer. (c) Summer rainfall distribution in East Asian continent and surrounding oceans and locations of loess sections, cave records and sediment cores referred to in the text. The new data in this paper come from IODP Site U1429 (red star). Data of summer rainfall amount (cm/month, July 2010) are from NCEP Reanalysis data of NOAA/OAR/ESRL PSD. (d) Potential sediment sources of IODP Site U1429. Yellow and red arrows indicate fine-grained and coarse-grained sediment input paths from Yellow River and Kyushu, respectively. Black dotted lines show the general boundaries of three regions in East Asia mentioned in this work. White line shows the coastal line during the Last Glacial Maximum (LGM). (For interpretation of the references to color in this figure legend, the reader is referred to the Web version of this article.)

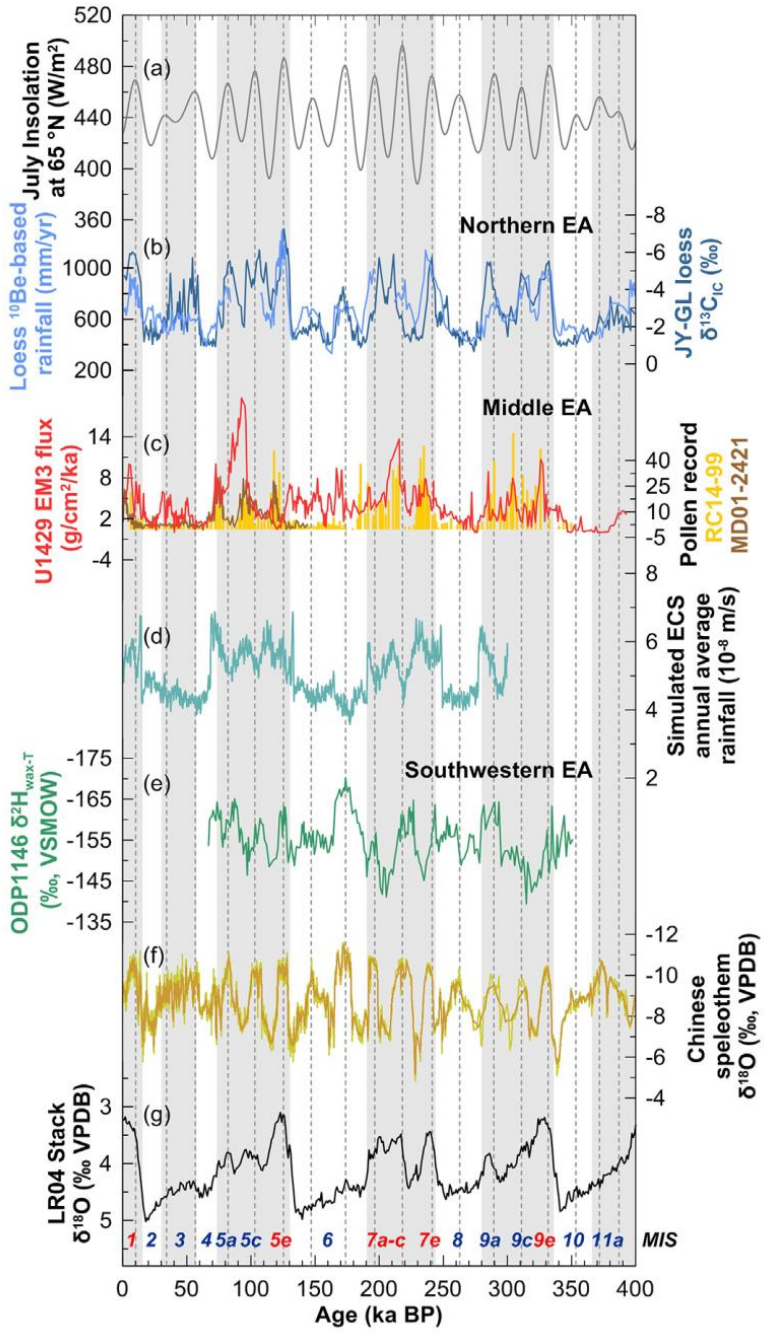

Figure 2. Time series of benthic $\delta^{18}O$ stack, summer insolation and rainfall in different regions of East Asia. (a) Northern hemisphere summer insolation at 65° N (Berger and Loutre, 1991). (b) Reconstructed northern East Asian rainfall by the ^{10}Be (Beck et al., 2018) and $\delta^{13}C$ of loess carbonate record (Sun et al., 2019). (c) Middle East Asian rainfall reconstructed by U1429 EM3 flux supplied from Kyushu, and pollen records from sediment cores RC14-99 (Morley and Heusser, 1997) and MD01-2421 (Igarashi and Oba, 2006) in eastern Japan. (d) Simulated East China Sea annual average rainfall (Clemens et al., 2018). (e) Precipitation d^2H in the Pearl River catchment (Thomas et al., 2014). (f) Chinese speleothem $\delta^{18}O$

record from Sanbao, Hulu and Dongge caves (Cheng et al., 2016). (g) Benthic $\delta^{18}O$ stack (Lisiecki and Raymo, 2005). Dotted lines highlight the intervals of maximum insolation. Transparent grey bars show the Marine Oxygen Isotope Stage (MIS). Marine isotope substages are indicated by red (interglacial intervals) and deep blue numbers (glacial intervals) (Past Interglacials Working Group of PAGES, 2016; Railsback et al., 2015).

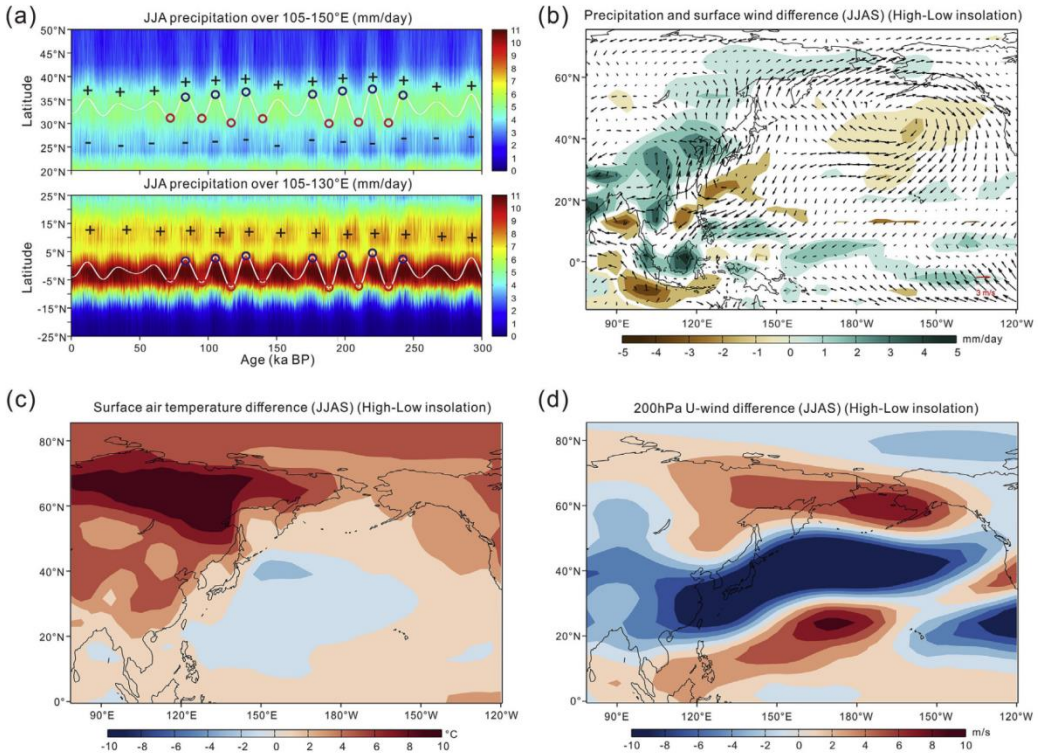

Figure 3. Simulated spatial and temporal change of rainfall, surface temperature and northern westerlies. (a) June-August rainfall distribution in the subtropical (20-50°N, 105-150°E) and tropical (25°S–25°N, 105-130°E) region during the last 300 ka. White curves indicate the precession. (b) June-September rainfall and surface wind difference between high and low insolation during the last 300 ka. (c, d) The same as b, but for the surface air temperature and 200 hPa U-wind differences, respectively. In b-d, the high and low insolation composites of mean climate are calculated based on seven periods of relatively stronger precession modulation, which are marked in red and blue circles.

9. 从一阶反转曲线推断深海沉积物静磁相互作用:相对古强度归一化的意义

翻译人：王敦繁 dunfan-w@foxmail.com

Yamazaki, T., ***Magnetostatic interactions in deep-sea sediments inferred from first-order reversal curve diagrams: Implications for relative paleointensity normalization, Geochem. Geophys. Geosyst.****, 2008. 9, Q02005, Doi:10.1029/ 2007GC001797.*

摘要：了解沉积物中的静磁相互作用对古地磁和岩石磁性很重要。已知静磁相互作用会显著影响非滞后剩磁(ARM)的获取效率，因此，可以通过静磁相互作用来控制ARM磁化率(cARM)与饱和等温剩磁(SIRM)的比值，后者是一种广泛用于环境应用的磁性粒度代理。相对古强度的估计也可能受到静磁相互作用的影响，因为 ARM 常被用作校正沉积物磁化率差异的一种正态器。本研究利用一阶反转曲线(FORC)图和 IRM 采集曲线对北太平洋深海沉积物中的磁性颗粒进行表征。结果表明，磁晶主要由一个非相互作用的单畴(SD)分量和一个相互作用的单畴(SD)分量组成，另外还有一个多畴(MD)分量。通过与局域相互作用场轴线平行的横截面曲线拟合，通过矫力峰半定量地估计了这些组分的相对丰度。假设相互作用场为高斯分布(Hu)，拟合三个分量。IRM 的采集曲线可以用对数高斯分布下的两个主导分量来描述。两组分的平均诱骗量分别为 40 ~100 mT。估计前者由生物磁铁矿携带，大致对应于 FORC 图导出的不相互作用的 SD 组分，后者由风成磁赤铁矿携带，对应于相互作用的 SD 组分。cARM/SIRM 比值随着相互作用的 SD 组分浓度的增加而降低。这意味着，cARM/SIRM 比值受到静磁相互作用的显著影响，而它不一定反映磁性颗粒的大小。静磁相互作用的影响在沉积物天然剩磁的携带不是很好理解,但如果是粒径同样敏感,规范化的结果相对古强度估计会过度补偿的磁性颗粒的浓度,导致归一化强度之间的一致性和标准化已经在文献中报道。

ABSTRACT: Understanding magnetostatic interactions in sediments is important for paleomagnetism and rock magnetism. Magnetostatic interactions are known to affect significantly the efficiency of anhysteretic remanent magnetization (ARM) acquisition, and hence the ratio of ARM susceptibility (cARM) to saturation isothermal remanent magnetization (SIRM), a magnetic grain-size proxy widely used for environmental applications, can be controlled by magnetostatic interactions. Relative paleointensity estimations may also be influenced by magnetostatic interactions because ARM is often used as a normalizer to correct for the difference in magnetizability of sediments. In this study, characterization of magnetic grains in deep-sea

sediments from the North Pacific Ocean was conducted using first-order reversal curve (FORC) diagrams and IRM acquisition curves. The FORC diagrams indicate that the magnetic grains consist mainly of a noninteracting single-domain (SD) component and an interacting SD component, and additionally of a multidomain (MD) component. The relative abundances of these components were semiquantitatively estimated by curve fitting of cross sections along a line parallel to the axis of local interaction fields (Hu) and through a peak in the coercivity (Hc). Three components were fitted assuming a Gaussian distribution of interaction fields (Hu). The IRM acquisition curves can be described by two dominant components assuming a log-Gaussian distribution. The mean coercivities of the two components are ~40 and ~100 mT, respectively. It is estimated that the former component is carried by biogenic magnetite, and roughly corresponds to the noninteracting SD component derived from the FORC diagrams, and that the latter component is carried by eolian maghemite, corresponding to the interacting SD component. The cARM/SIRM ratio decreases with increasing concentration of the interacting SD component. This implies that the cARM/SIRM ratio is significantly affected by magnetostatic interactions and that it does not necessarily reflect magnetic grain size. The effect of magnetostatic interactions on natural remanent magnetization acquisition in sediments is not well understood, but if it is similarly sensitive to the SIRM, normalization by ARM in relative paleointensity estimations would overcompensate for the concentration of magnetic grains and cause the significant coherence between the normalized intensity and the normalizer that has been reported in the literature.

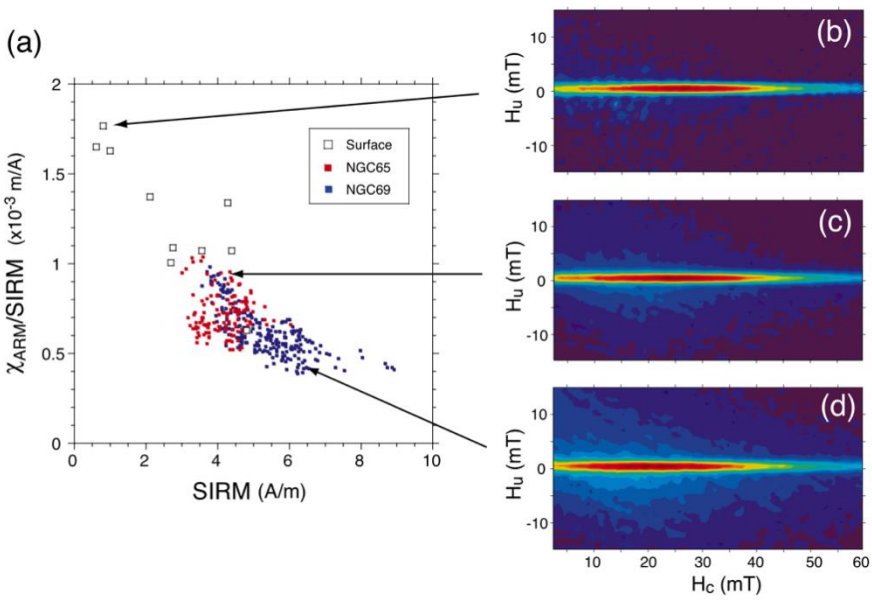

Figure 1. (a) Relationship between cARM/SIRM ratio (anhysteretic remanent magnetization

susceptibility to saturation isothermal remanent magnetization) and SIRM. FORC diagrams for representative samples on the right- hand side are for specimens from depths of (b) 0.04 m in surface sediments from grab-sample NK5, (c) 4.18 m in core NGC65, and (d) 1.31 m in core NGC69. A total of 191 FORCs were measured, and a smoothing factor (SF) of 3 was used [Roberts et al., 2000].

10. 马尔马拉海沉积物在过去 70 ka 来的高分辨率古地磁记录

翻译人：王浩森 11930841@mail.sustech.edu.cn

Makaroğlu Ö, Nowaczyk N R, Eriş K K, et al. ***High-resolution palaeomagnetic record from Sea of Marmara sediments for the last 70 ka[J]. Geophysical Journal International,*** *2020. 222: 2024-2039. https://doi.org/10.1093/gji/ggaa281*

摘要：对从马尔马拉海回收的两个沉积岩芯进行了磁性地层学和地球化学分析，以研究最近 70 ka 期间的地磁场变化。根据 8 个 AMS ^{14}C 年龄点，年代学和利用格陵兰岛冰芯氧同位素数据中的 Ca 浓度来校准两个岩芯中每个岩芯的年代。根据年龄模型， MD01-2430 和 MRS-CS19 分别可恢复到 70 和 32 ka。 MD01－2430 岩芯的平均沉积速率为 43 cm kyr－1，MRS CS19 岩芯的平均沉积速率为 68 cm kyr－1，可以进行马尔马拉海的地磁场变化高分辨率重建工作。磁性矿物对该地区的冰川静态海平面变化和古气候变化敏感，反映了最近 70 ka 期间马尔马拉海古生物环境的变化。尽管在某些地层间隔中古地磁记录由于早期成岩作用受到了破坏，但马尔马拉海沉积物中的相对古强度变化与来自其他地区（例如附近的黑海和 GLOPIS-75）的类似记录有很好的相关性。来自马尔马拉海岩芯的方向记录显示出典型的古强度变化模式，变化异常在 41 和 18 ka，分别代表 Laschamps 和假定的 Hilina Pali 偏移。两个方向异常也与古强度最小值相关。最低的 34.5 ka 的古强度可能与 Mono 湖的偏移有关，到目前为止，马尔马拉海以上的古磁记录中没有记录到任何方向偏差。

ABSTRACT: Magnetostratigraphic and geochemical analyses were performed on two sediment cores recovered from the Sea of Marmara to investigate geomagnetic field variations over the last 70 ka. A chronology for each of the two cores was developed from eight AMS 14C datings, tephrochronology, and tuning of Ca concentrations with stadials and interstadials observed in Greenland ice core oxygen isotope data. Based on the age models, cores MD01–2430 and MRS-CS19 reach back to 70 and 32 ka, respectively. High average sedimentation rates of 43 cm kyr–1 for core MD01–2430 and 68 cm kyr–1 for core MRS CS19 allow high-resolution reconstruction of geomagnetic field variations for the Sea of Marmara. Mineral magnetic properties are sensitive to glacioeustatic sea level changes and palaeoclimate variations in this region, reflecting the variable palaeoenvironmental conditions of the Sea of Marmara during last 70 ka. Despite the impairment of the palaeomagnetic record in some stratigraphic intervals due to early diagenesis, relative palaeointensity variations in the Sea of Marmara sediments correlate well with similar records derived from other regions, such as the nearby Black Sea and the GLOPIS-75 stack. The directional record derived from the Sea of Marmara cores exhibits typical palaeosecular variation patterns, with directional anomalies at 41 and 18 ka, representing the Laschamps and postulated Hilina Pali excursions, respectively. Both directional anomalies are also associated with palaeointensity minima. A further palaeointensity minimum at 34.5 ka is likely related to theMono Lake excursion, with no directional deviation documented in the Sea of Marmara palaeomagnetic record so far.

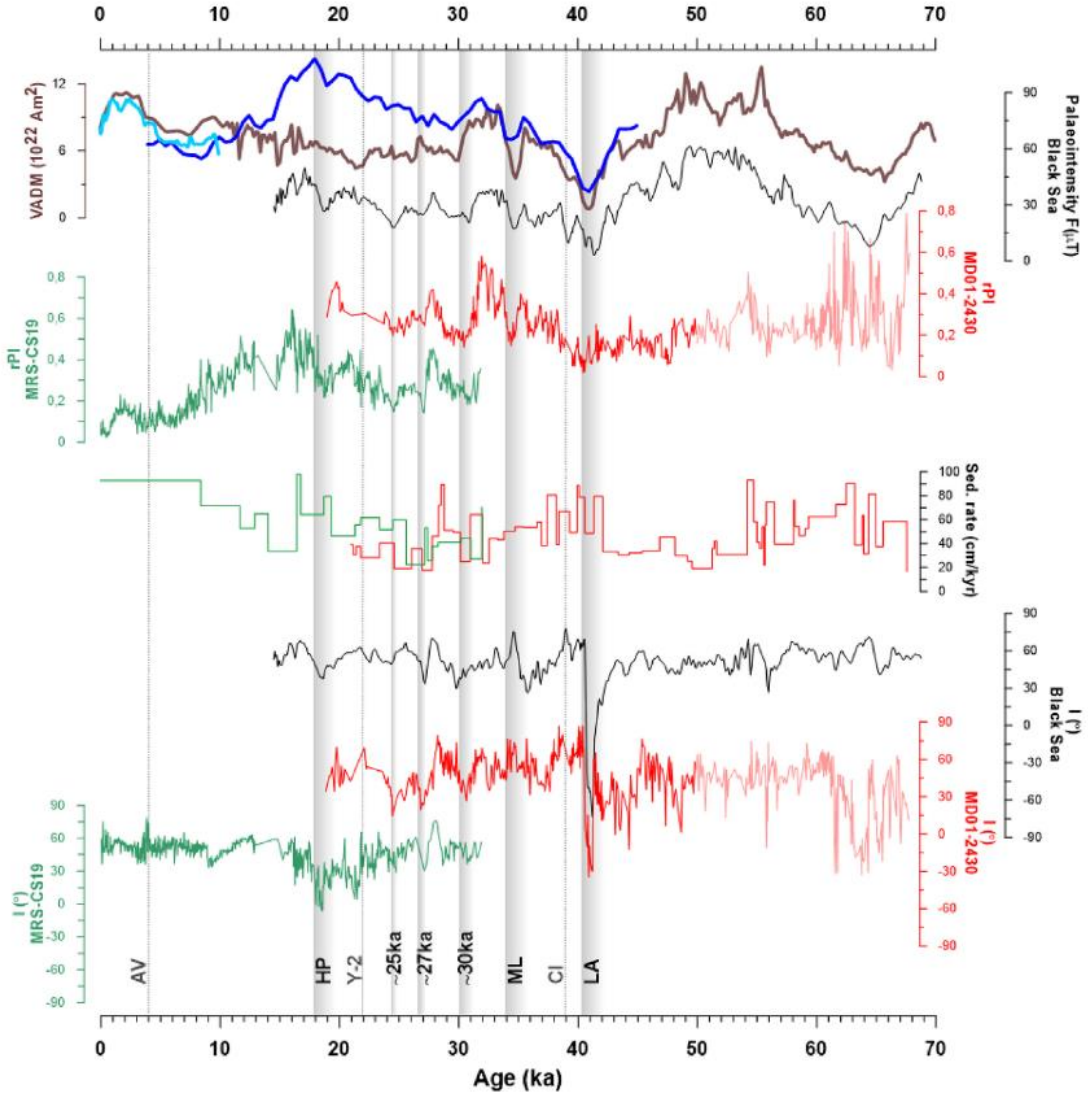

Figure 1. Palaeointensity and inclination records from cores MRS-CS19 (green) and MD01–2430 (red) over the last 70 ka. For comparison, the palaeomagnetic record from the Black Sea (black; Liu *et al.* subm.), the GLOPIS-75 record (brown; Laj *et al.* 2004), VADM stack (blue; Channell *et al.* 2018), and Holocene model (light blue; Korte *et al.* 2011) are also shown. Light red line shows unreliable RPI record of core MD01–2430. Vertical grey bars denote magnetic field excursions, LA (Laschamps), ML (Mono Lake) and HP (Hilina Pali). The dotted vertical lines mark the stratigraphic positions of the Avellino (AV), Cape Riva (Y-2) and Campanian Ignimbrite tephra (CI/Y-5) in the studied cores.

11. 非人为沉积物重建的洞穴演化史有助于我们理解相关的考古背景

翻译人：郑威 11930589@mail.sustech.edu.cn

Karkanas P, Marean C, Bar-Matthews M, et al. ***Cave life histories of non-anthropogenic sediments help us understand associated archaeological contexts****[J].* ***Quaternary Research****, 2020. 1-20. https://doi.org/10.1017/qua.2020.72*

摘要：品尼高点临近南非西开普敦省莫塞尔湾，因拥有一系列有重要考古发现的洞穴而闻名。其中两个洞穴（PP13B和PP5-6）的详细发掘和研究记录了人为作用主导和地质作用主导沉积的时期。各种洞穴都没有人类残留的证据。我们详细研究了三个洞穴（Staircase洞、Crevice洞、以及PP29洞），这些洞穴形成的地质和沉积条件与有人类活动的洞穴相同。这三个洞穴和大多数品尼高点的洞穴一样有大量洞穴沉积物，并对沉积物做了古气候和古环境重建的同位素分析。这些洞穴也为了解品尼高点当地原始的地质成因的信号提供了机会，从而为研究人为成因的洞穴沉积物提供了一个地质背景白板。考古学家通常只关注有强烈人类活动信号的遗址，但是，通过建立洞穴演化史，我们可以在来龙去脉的背景认知上更上一层楼。

ABSTRACT: Pinnacle Point (PP) near Mossel Bay in the Western Cape Province, South Africa, is known for a series of archaeological caves with important archaeological finds. Extensive excavations and studies in two of them (PP13B and PP5-6) have documented alternating periods of anthropogenic-dominated and geogenic-dominated sedimentation. A variety of caves do not bear evidence of anthropogenic remains. We have studied in detail the remnant deposits of three of them, Staircase Cave, Crevice Cave, and PP29, which have been formed under the same geologic and sedimentary conditions with those with anthropogenic contributions. Their remains are small and patchy but have extensive speleothem formations (as do most caves at PP) that were isotopically analyzed for paleoclimate and paleoenvironmental reconstruction. These caves also offer the opportunity to understand the purely geogenic signature of the PP locality and thus offer a geogenic baseline for the anthropogenic caves. Archaeologists normally focus only on sites with strong anthropogenic signals, but by building cave life histories we “raise the bar” (Goldberg 2008, p. 30) on our contextual knowledge.

.

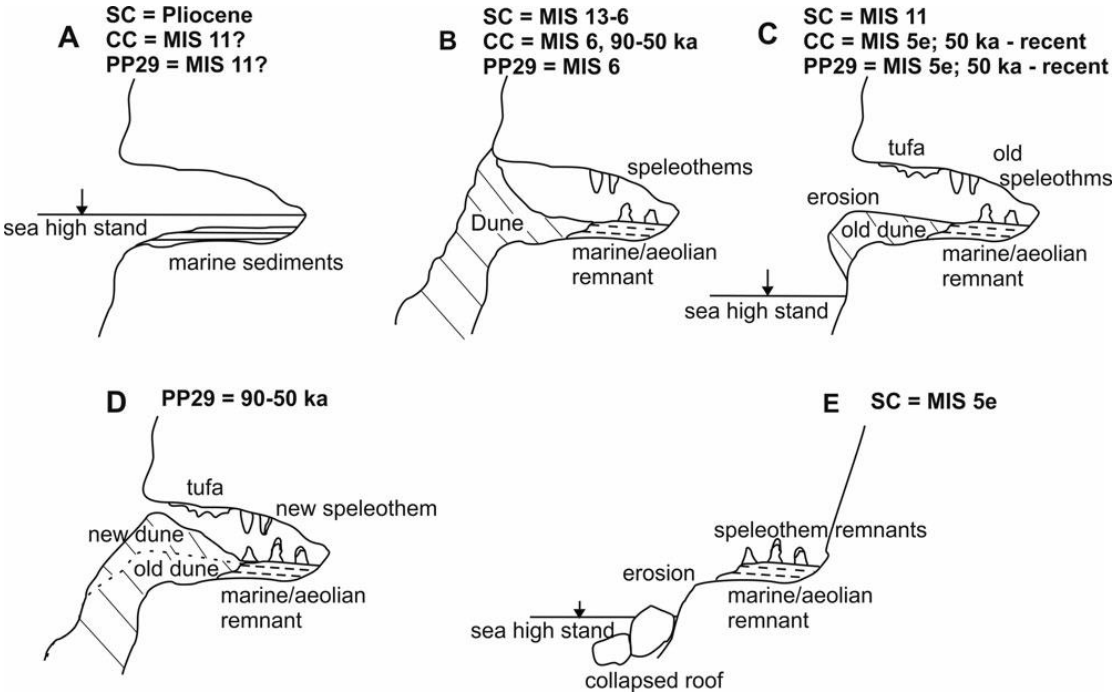

Figure 1. History of caves and their phases. The caves and the age period that correspond to each phase are also shown. (A) Cave formation by a sea high stand and occasional deposition of marine sediments. (B) Retreat of sea. Blocking of cave entrance by dunes: formation of speleothems. (C) Sea high stand close to the level of the cave. Erosion of dune sediment and any other previous deposit: formation of tufa. (D) Retreat of sea. New dunes blocking partially the cave: occasional formation of new speleothems. (E) Sea high stand close to the level of the cave. Erosion and Collapse of cave roof and exposure of its sedimentary fill. Circled Phases C and D denote periods when human occupation is possible, as observed in other Pinnacle Point (PP) caves. CC, Crevice Cave; PP29, PP29 Cave; SC, Staircase Cave.

12. 26 ka 以来中亚的干湿演化:来自西部天山吉尔吉斯黄土剖面的见解

翻译人：李海 12031330@mail.sustech.edu.cn

Li, Y., Y. Song, R. Orozbaev, J. Dong, X. Li and J. Zhou 2020. **Moisture evolution in Central Asia since 26 ka: Insights from a Kyrgyz loess section, Western Tian Shan[J]. Quaternary Science Reviews**, 2020. 249: 106604. https://doi.org/10.1016/j.quascirev.2020.106604

摘要: 中亚地处欧亚大陆腹地，在当前全球变暖趋势下，面临着持续变暖的极端风险。古气候研究为预测中亚地区未来的气候变化提供了必要的参考。然而，对中亚地区气候变化机制的了解较少。在这里，我们利用 26 ka 以来天山西部的黄土剖面记录来研究该区的干湿变化。利用 GSIm 与 ΔL∗重建天山西部的风力及湿润程度。由于成土作用弱或其他因素的影响，频率磁化率、红度及黄度未能提供可靠的气候信息。GSIm 的记录显示，在降水量为~15 ka 之前的夏季降水达到最大值，在降水量为~15 ka 之后的春季降水达到最大值，这很可能与北半球冰盖退缩对纬度气候区和大气环流的大规模调节有关。基于 ΔL∗记录，我们将重点放在温度调制蒸发水分作用对中亚地区干湿程度的演化；但这只影响了春季和夏季的干湿演化，对冬季的干湿程度影响不大。此外，ΔL∗记录也表明大气湿度可以一定程度上影响了长期有效的湿度变化。

Abstract: Central Asia (CA) is located in the hinterland of the Eurasian continent, and faces an extreme risk of continued aridification under the current global warming trend. To predict future climate change in CA, paleoclimate studies provide essential references. However, the mechanisms underlying climate changes in CA remain relatively poorly known. Here, we investigate moisture variations in CA, as recorded in a 6-m loess section in the Western Tian Shan, Kyrgyzstan, which has accumulated since ~26 ka based on the radiometric AMS^{14}C dating. We reconstructed the evolution of the wind regime and moisture conditions in the Western Tian Shan with a modified grain size index (GSIm) and a new L∗ proxy (ΔL∗). While the frequency-dependent magnetic susceptibility (χfd), redness (a∗) and yellowness (b∗) did not provide reliable paleoclimatic indicators, due to weak pedogenesis and other controlling factors. The GSIm records demonstrated a precipitation maximum in summer before ~15 ka, shifting to a maximum in spring after ~15 ka, probably associated with large-scale modulation of the latitudinal climatic zones and atmospheric circulation in response to retreat of the Northern Hemisphere ice sheets. Based on the ΔL∗ records, we place emphases on the important role of temperature-modulated evaporation in moisture evolution across CA; however, this has only influenced moisture evolution in spring and summer, with little effect on winter moisture conditions. Moreover, the ΔL∗ records may also indicate that atmospheric humidity can partly affect the long-term effective moisture variations.

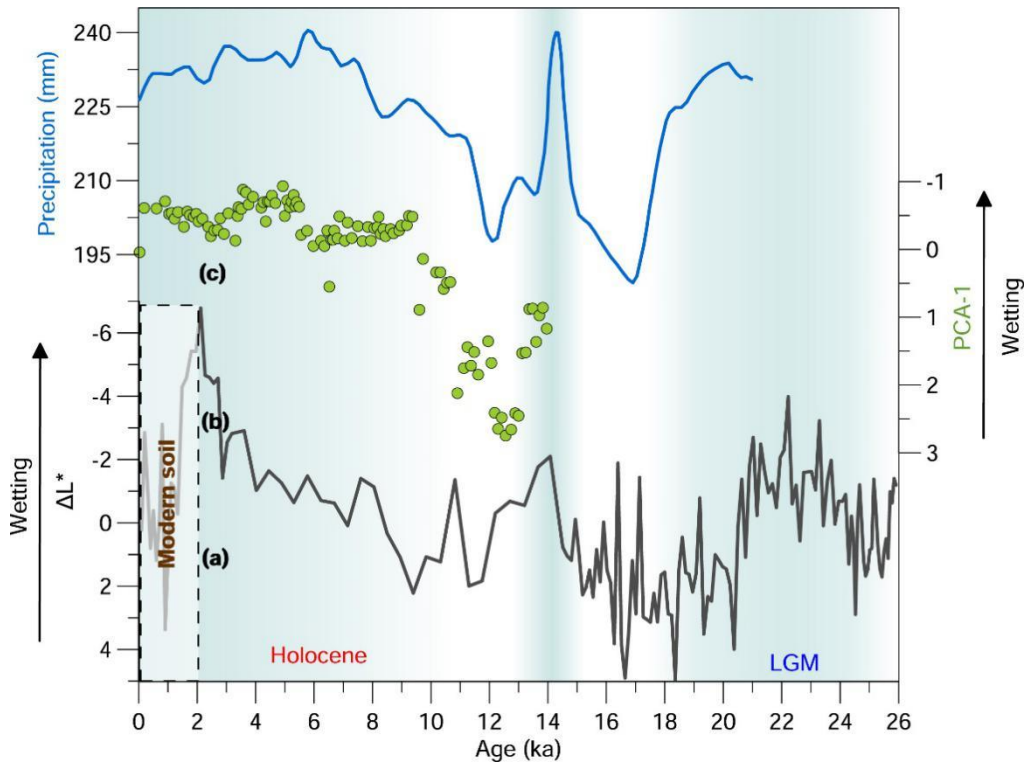

Fig. 1 Comparisons of moisture proxy ΔL∗ (a) with the first principal component (PCA-1) generated by principal component analysis (PAC) of the pollen data from the Sayram Lake sediment core (Jiang et al., 2013a) (b) and mean annual precipitation averaged over 35°–50° N and 50°–70° E based on the TraCE-FULL simulation (Zhang et al., 2018) (c).

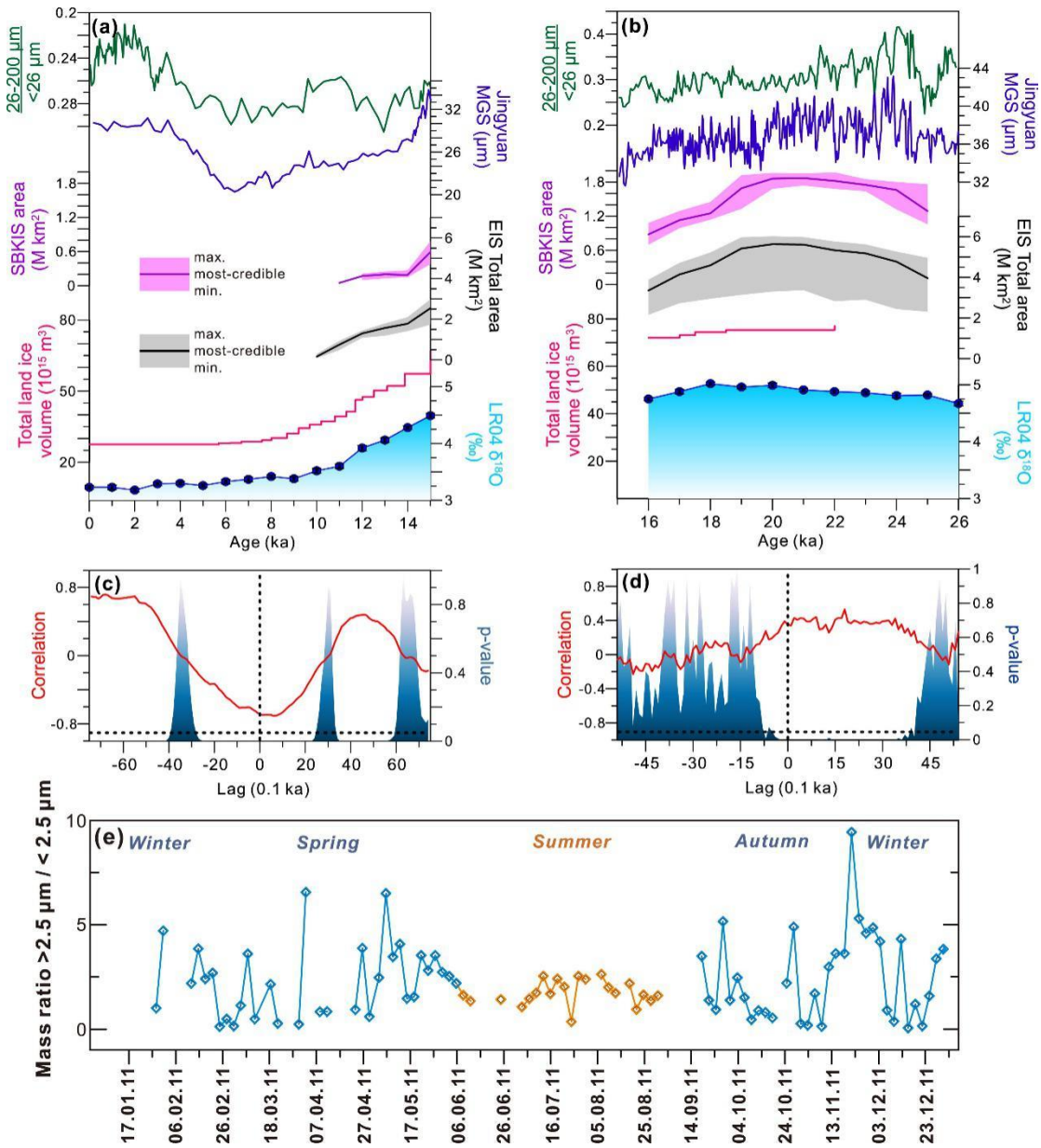

Fig. 2 (a), (b) Comparisons of GSIm [(26–200 µm)/<26 µm] in the BSK loess, mean grain sizes (MGS) of Jingyuan loess in the western CLP (Sun et al., 2010), the area of the Eurasian ice sheets (EIS) and the Svalbard-Barents-Kara Ice Sheet (SBKIS) (Hughes et al., 2016), total land ice volume from ice sheets in the TraCE simulation (Lora et al., 2016) and benthic δ18O record [LR04, Lisiecki and Raymo (2005)] since 26 ka; (c), (d) cross-correlation analyses between the BSK GSIm and Jingyuan MGS for 0–15 ka and 15–26 ka respectively; (e) time series of the average mass ratios of the >2.5 µm fraction and the <2.5 µm fraction for the 3-day sampling intervals in 2011 [modified after Schettler et al. (2014)]. Dashed lines in (c) and (d) mark the 0.05 p-value.

13. 全球温度模式揭示了全新世温度难题

翻译人：张亚南 zhangyn3@mail.sustech.edu.cn

Jurgen Bader, Johann Jungclaus, Natalie Krivova et al., ***Global temperature modes shed light on the Holocene temperature conundrum*** *[J].* ***Nature Communications****, 2020, 11, 4726.*

https://doi.org/10.1038/s41467-020-18478-6

摘要：全新世全球年均温度演变的重建结果有所冲突。一些重建结果显示晚全新世全球气温变冷，而另一重建结果又表明全球变暖。我们的研究表明在利用瞬态气候模型模拟的数据进行全新世年均温度的时空变化时，全球变暖和降温模式都会出现。这种变暖模式在热带地区最为显著；而模拟到的降温模式则受控于北极海冰季节性周期变化，后者受到轨道变化和火山爆发的影响。全新世中期以变暖模式为主，在晚全新世则被降温模式所替代。两种气温变化模式的加权和得出模拟的全球温度变化趋势。本研究对指标数据的解释和选择指标区域位置来计算全球平均温度具有重要的启示。

ABSTRACT: Reconstructions of the global mean annual temperature evolution during the Holocene yield conflicting results. One temperature reconstruction shows global cooling during the late Holocene. The other reconstruction reveals global warming. Here we show that both a global warming mode and a cooling mode emerge when performing a spatio-temporal analysis of annual temperature variability during the Holocene using data from a transient climate model simulation. The warming mode is most pronounced in the tropics. The simulated cooling mode is determined by changes in the seasonal cycle of Arctic sea-ice that are forced by orbital variations and volcanic eruptions. The warming mode dominates in the mid-Holocene, whereas the cooling mode takes over in the late Holocene. The weighted sum of the two modes yields the simulated global temperature trend evolution. Our findings have strong implications for the interpretation of proxy data and the selection of proxy locations to compute global mean temperatures.

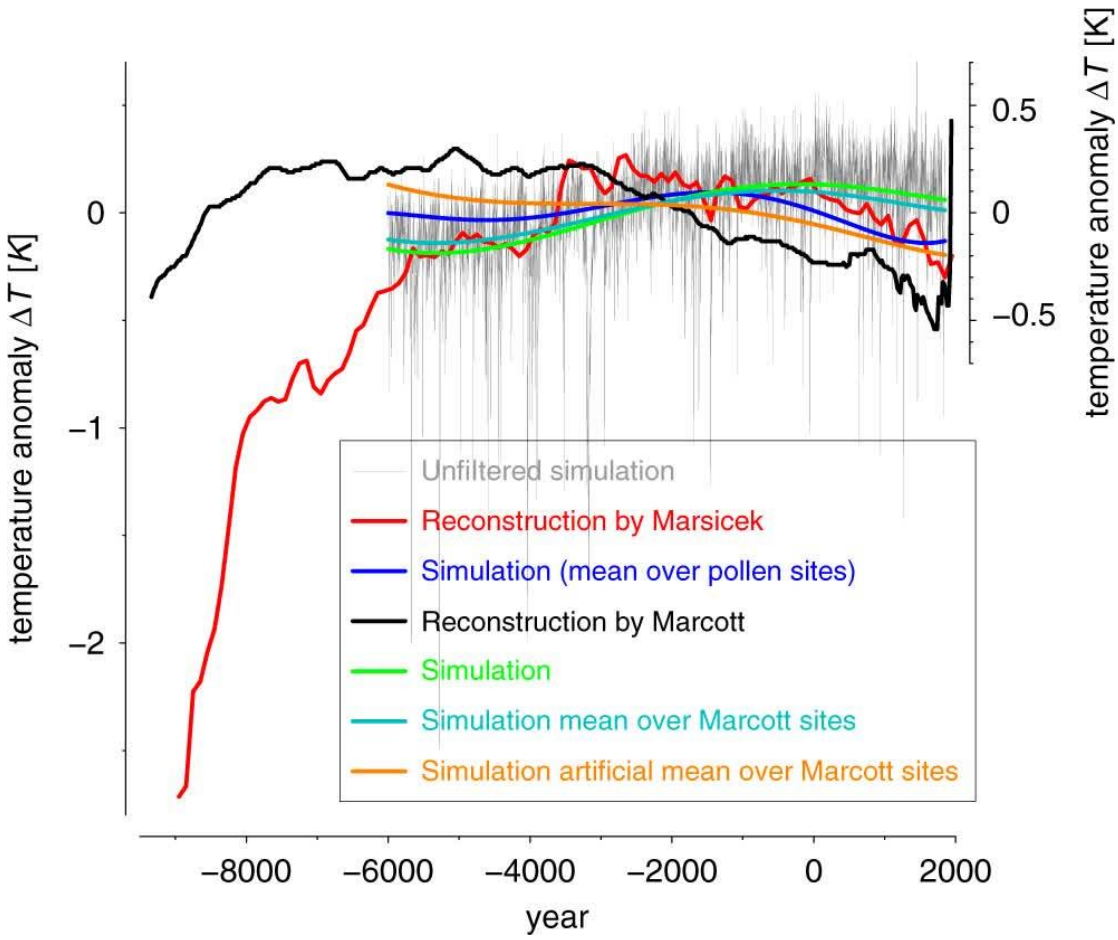

Figure 1. Annual global-mean temperature anomaly during the Holocene based on reconstructions and a transient simulation. The annual global mean temperature anomaly based on the reconstructions by Marcott (black curve), based on the reconstruction by Marsicek (red curve), based on the transient unfiltered simulation (gray curve), based on the low-pass filtered simulation (green curve), based on the low-pass filtered simulation over the pollen sites used for the Marsicek reconstruction (blue curve), based on the low-pass filtered simulation over the Marcott sites (cyan), and based on an artificial simulation dataset over the Marcott sites (orange). All time series have been adjusted to the simulation time period (6000 BCE to 1850 CE). The units are Kelvin. The y-axis on the left side also shows the temperature anomaly but with a finer scale for easier comparison of the curves over the last millennia. For the computation for the artificial simulation dataset please see text for details.

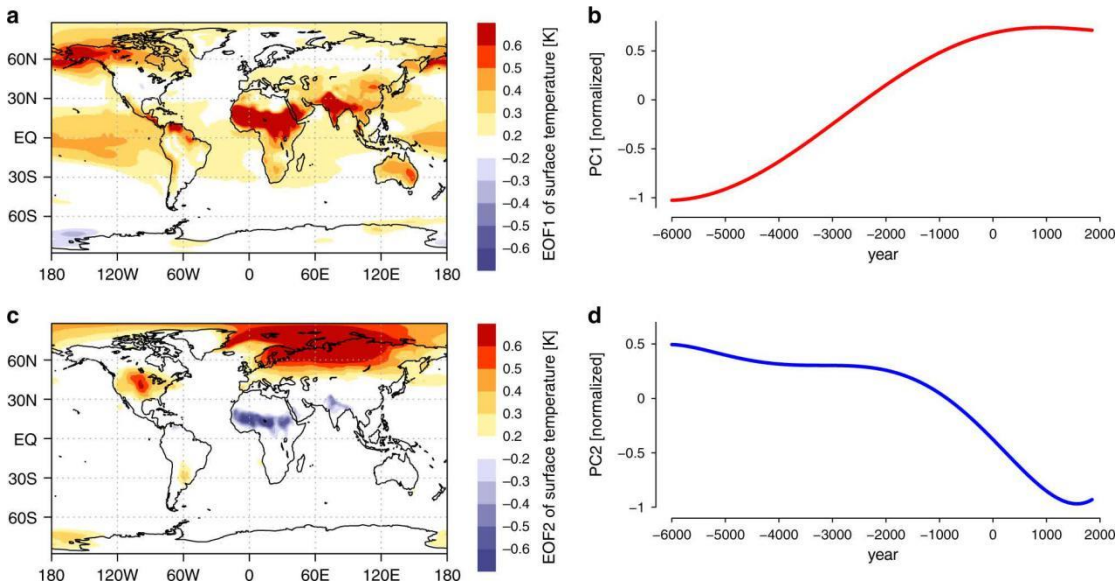

Figure 2. The simulated warming and cooling mode in the transient Holocene simulation. First two spatial empirical orthogonal function (EOF) modes (a,c) and corresponding normalized smoothed principal components (PCs) (b,d) based on the simulated annual 2 m temperature using the MPI-ESM data. The red and blue curves in the right panels show the low-pass filtered PCs. The explained variances of the annual (not low-pass filtered) temperature modes are: 18% and 9%. Panels (a) and (b) show the spatial pattern and temporal evolution of the warming mode and panels (c) and (d) correspond to the cooling mode.

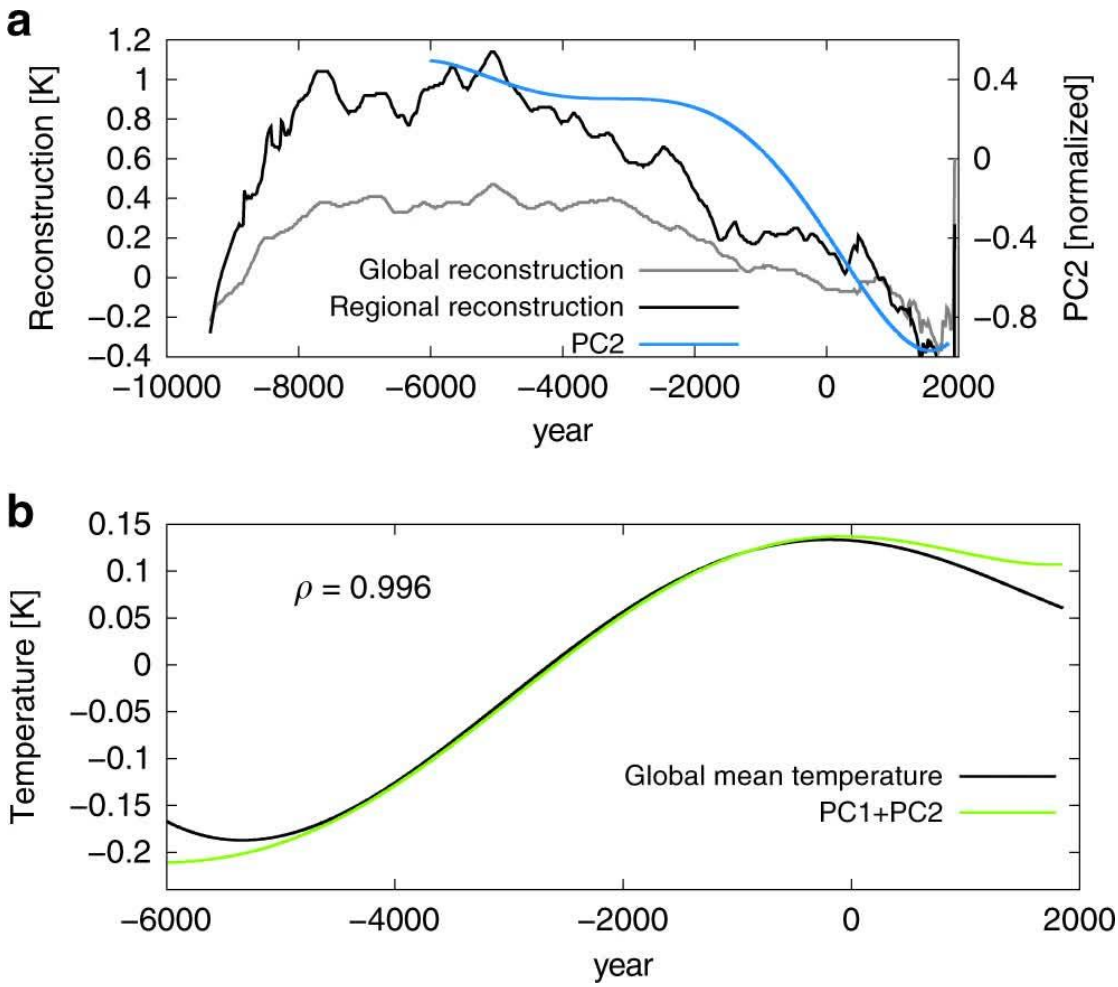

Figure 3. Net effect of the warming and cooling mode explains the long-term temperature trends during the Holocene. a Temperature reconstructions based on Marcott et al. 2013 (gray and black curve) and the cooling mode (PC2) (blue curve). The gray curve shows the global mean temperature whereas the black curve shows a regional mean from 30°N poleward. b Low-pass filtered simulated annual global mean temperature anomaly (black curve) and sum of the weighted warming (PC1) and cooling (PC2) mode (green curve). The PCs have been weighted by the global means of the corresponding spatial patterns before summation. The global mean of EOF1 is about 0.238 K and of EOF2 it is about 0.066 K. ρ is the correlation coefficient between the two curves.

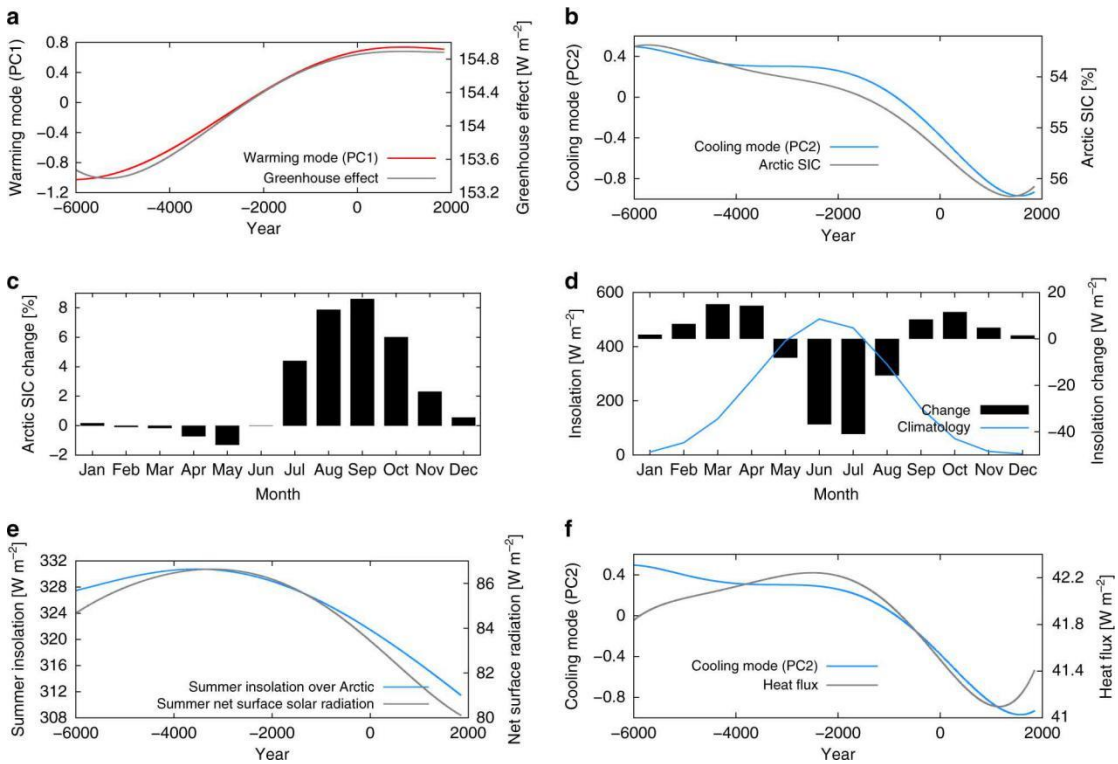

Figure 4. Time evolution of the warming mode is correlated with the greenhouse effect while the cooling mode is associated with the Arctic sea-ice increase. a The gray curve shows the low-pass filtered greenhouse effect and the red curve the low-pass filtered warming mode (PC1). The greenhouse-gas effect is defined as the difference between the upward surface thermal radiation and the outgoing longwave radiation at the top of the atmosphere [Wm−2]. b Low-pass filtered normalized cooling-mode (PC2) and low-pass filtered annual Arctic sea-ice concentration (SIC) in %. Please note that the right y-axis is flipped. c Change in the seasonal cycle of the Arctic SIC between the first and last one hundred years of the simulation. d Blue curve shows the simulated climatological insolation. Bars indicate the change in the seasonal cycle of the insolation between the first and last one hundred years of the simulation. e Low-pass filtered summer (JAS) insolation (blue curve) and summer (JAS) net surface solar radiation (black curve). f The gray curve shows the area-averaged heat flux from the ocean to the atmosphere in Wm−2 and the blue curve the cooling mode (PC2). Except for the warming mode (PC1), the cooling mode (PC2) and the greenhouse effect all data is area-averaged from 60° poleward.